Light absorption properties and potential sources of particulate brown carbon in the Pearl River Delta region of China

Zhujie Li[1,2], Haobo Tan[2]*, Jun Zheng[1]*, Li Liu[2,3], Yiming Qin[4], Nan Wang[2], Fei Li[2], Yongjie Li[5], Mingfu Cai[3], Yan Ma[1], and Chak K. Chan[4]

[1]Collaborative Innovation Center of Atmospheric Environment and Equipment Technology, Nanjing University of Information Science and Technology, Nanjing, China

[2]Key Laboratory of Regional Numerical Weather Prediction, Institute of Tropical and Marine Meteorology, China Meteorological Administration, Guangzhou, China

[3]Department of Atmospheric Science, Sun yat-sen University, Guangzhou, China

[4]School of Energy and Environment, City University of Hong Kong, Hong Kong, China

[5]Department of Civil and Environmental Engineering, Faculty of Science and Technology, University of Macau, Macau, China

Correspondence to: Haobo Tan (hbtan@grmc.gov.cn) and Jun Zheng (zheng.jun@nuist.edu.cn)

19   **Abstract:**

20   Brown carbon (BrC) is a special type of organic aerosols (OA), capable of absorbing solar

21   radiation from near-ultraviolet (UV) to visible wavelengths, which may lead to an increased

22   aerosol radiative effect in the atmosphere. While high concentrations of OAs have been

23   observed in the Pearl River Delta (PRD) region of China, the optical properties and

24   corresponding radiative forcing of BrC in the PRD are still not well understood. In this work,

25   we conducted a set of comprehensive measurements of atmospheric particulate matter from 29

26   November 2014 to 2 January 2015 to investigate aerosol compositions, optical properties,

27   source origins and radiative forcing effects at a suburban station in Guangzhou. The particle

28   absorption Ångström exponent (AAE) was deduced and utilized to differentiate light absorption

29   by BrC from that by black carbon (BC). The results showed that the average absorption

30   contributions of BrC were 34.1±8.0% at 370 nm, 23.7±7.3% at 470 nm, 16.0±6.7% at 520 nm,

31   13.0±5.4% at 590 nm and 8.7±4.3% at 660 nm. A sensitivity analysis of the evaluation of the

32   absorption Ångström exponent of BC (AAE_{BC}) was conducted based on the Mie theory

33   calculation assuming that the BC-containing aerosol was mixed with the core-shell and external

34   configurations. The corresponding uncertainty in AAE_{BC} was acquired. We found that

35   variations in the imaginary refractive index (RI) of the BC core can significantly affect the

36   estimation of AAE_{BC}. However, AAE_{BC} was relatively less sensitive to the real part of the RI

37   of the BC core and was least sensitive to the real part of the RI of the nonlight absorbing shell.

38   BrC absorption was closely related to aerosol potassium cation content (K^+), a common tracer

39   of biomass burning emissions, which was most likely associated with straw burning in the rural

40   area of the western PRD. Diurnal variation in BrC absorption revealed that primary organic

41   aerosols had a larger BrC absorption capacity than secondary organic aerosols (SOAs).

42   Radiative transfer simulations showed that BrC absorption may cause 2.3±1.8 W m^{-2} radiative

43   forcing at the top of the atmosphere (TOA) and contribute to 15.8±4.4% of the aerosol warming

44   effect. A chart was constructed to conveniently assess the BrC radiative forcing efficiency in

45   the studied area with reference to certain aerosol single-scattering albedo (*SSA*) and BrC

46   absorption contributions at various wavelengths. Evidently, the BrC radiative forcing efficiency

47   was higher at shorter wavelengths.

Keywords: Brown carbon, Black carbon, Absorption Ångström exponent, Radiative forcing, Pearl River Delta.

48 **1 Introduction**

49 Black carbon (BC) and organic carbon (OC) are dominant carbonaceous aerosol components

50 that mainly originate from biomass burning in a global scale (Bond et al., 2004) and have

51 attracted great environmental concerns in rapidly developing regions. Carbonaceous aerosols

52 can not only exert adverse impacts on public health, similar to other particulate matters, but

53 also significantly affect the terrestrial radiation balance with enormous uncertainties. In

54 previous studies, BC was often considered to be the only light-absorbing species (Andreae and

55 Gelencser, 2006), and OC was believed to only be able to scatter light, i.e., causing a cooling

56 effect (Bond et al., 2011). Nevertheless, it has been reported that some fraction of organic

57 aerosols (OAs) may also specifically contribute to light absorption from the near-ultraviolet

58 (UV) to visible wavelength range, which is referred to as brown carbon (BrC) (Kirchstetter et

59 al., 2004). BrC optical properties are strongly affected by its chemical composition and physical

60 structure, which are related to different BrC sources. BrC can originate not only from direct

61 emissions, including smoldering, biomass burning or any type of incomplete fuel combustion

62 process (T. C. Bond et al., 1999;Cheng et al., 2011), but also from secondary organic aerosol

63 formation processes, such as aqueous phase reactions in acidic solutions (Desyaterik et al., 2013)

64 or volatile organic compound (VOC) oxidation (Laskin et al., 2015;Sareen et al., 2010). In

65 addition, BrC could have a complicated molecular composition and intermix with other

66 substances, such as BC, non-absorbing OAs and other inorganic materials, making it

67 complicated to investigate BrC optical properties.

68 BC absorption is commonly assumed to be covering the full wavelength-range. However, the

69 light absorption property of BrC is believed to be more wavelength-dependent, which can be

70 represented by distinct absorption Ångström exponent (AAE) values, i.e., the power exponent

71 of the light absorption coefficient. A typical threshold for the AAE of BC (AAE_{BC}) of 1.6 has

72 been recommended to distinguish BrC from BC (Lack and Cappa, 2010), and the AAE of BrC

73 has been reported as having a wider range (2 to 7) (Hoffer et al., 2005). Based on the difference

74 in the wavelength dependence of light absorption between BC and BrC, previous studies have

75   applied the AAE method to differentiate light absorption by BrC through multiwavelength

76   optical measuring apparatus, such as 3-wavelength Photoacoustic Soot Spectrometer (PASS-3)

77   (Lack and Langridge, 2013), multiwavelength Aethalometer (Olson et al., 2015), etc. Based on

78   the AAE method, the BrC absorption contribution has been estimated to be approximately 6 to

79   41% of total aerosol light absorption at short wavelengths, e.g., at 370 nm and 405 nm

80   (Washenfelder et al., 2015). A uniform AAE_{BC} from ~300 nm up to ~700 nm (Moosmüller et

81   al., 2011) is commonly used when evaluating the BrC absorption contribution using the AAE

82   method. However, it has been reported that the AAE_{BC} can be influenced by the mixing state,

83   BC core size and morphology (Lack and Cappa, 2010). The lensing effect of the coating shell

84   may enhance BC light absorption, the magnitude of which may also depend on wavelength and

85   can alter the value of AAE_{BC} (Liu et al., 2018). Moreover, different values of AAE_{BC} have been

86   found in the near-infrared and UV ranges (Wang et al., 2018). Therefore, using the default value

87   of $AAE_{BC} = 1$ may lead to uncertainty in BrC absorption coefficient estimation.

88   Quantifying BrC optical absorption accurately is essential to interpret aerosol optical depth

89   (AOD), and the corresponding aerosol direct radiative forcing (DRF) on the atmosphere can

90   also be evaluated if the single-scattering albedo (*SSA*) and extinction coefficient of aerosols are

91   known. The estimation of the DRF of BrC has shown a distinct seasonal variation, indicating

92   the influence of different absorption properties of BrC (Arola et al., 2015). A global simulation

93   study indicated that the average warming effect at the TOA caused by BrC absorption can be

94   up to 0.11 W m^{-2}, corresponding to ~25% of that predicted from BC absorption only (Feng et

95   al., 2013).

96   During the last three decades, rapid economic development has led to severe air pollution

97   problems in the PRD region (Chan and Yao, 2008). With rapid increases in the automobile

98   population and factories, high loadings of SOAs have often been observed (Tan et al., 2016b).

99   Biofuel usage may also play a significant role during wintertime air pollution events in the PRD,

100   indicating that the contribution from BrC light absorption cannot be ignored (Wu et al., 2018).

101   Recently, BrC light absorption has been quantified by Qin et al. (2018) using the AAE method

102   in the PRD region. OA chemical composition was simultaneously measured by a high-

103   resolution time-of-flight aerosol mass spectrometer, and it was found that organic aerosols

104   originating from biomass burning possessed the most intense absorption capability and were

largely responsible for BrC absorption. Qin et al. (2018) also suggested that correlations

between OA chemical compositions and BrC absorption were wavelength-dependent.

In this paper, we applied the homologous AAE differentiation method to quantify the fraction

of aerosol light absorption by BrC using the measurements from a seven-wavelength

Aethalometer. The potential error incurred with this methodology was determined using Mie

theory simulations, especially for various complex refractive indexes of the BC core and the

coating material. The correlation between BrC light absorption and water-soluble ions, which

is used as the source tracer, was employed to identify potential BrC sources. An atmospheric

radiative transfer model has also been applied to evaluate the impact of BrC on direct radiative

forcing using surface-based aerosol optical properties and satellite-based surface-albedo data.

The magnitudes of aerosol radiative forcing at the top of the atmosphere due to BC and BrC

were also individually quantified.

2 Methodology

2.1 Sampling site

Field observations were conducted at the Panyu station (113°21′E, 23°00′N), which is a

monitoring site of the Chinese Meteorological Administration (CMA) Atmospheric Watch

Network (CAWNET) that is located on the summit of Dazhengang Mountain (approximately

150 m above sea level) in Guangzhou, China. Figure 1 shows the location of the Panyu site,

which is situated at the center of the PRD and is separated from residential areas by at least 500

m. Some agricultural fields can be found to the west of the site. Although there were no

significant pollution sources nearby, this suburban site was strongly affected by pollutants

transported from the urban area of Guangzhou and crop residual fires transported from the rural

area of the PRD. The field campaign was conducted from 29 November 2014 to 2 January 2015.

During the measurement period, aerosol light scattering and extinction, BC concentration,

particle number size distribution (PNSD), OC concentration, and the water-soluble ion

concentrations of $PM_{2.5}$ were continuously monitored.

2.2 Measurements and data analysis

All instruments were housed inside the 2nd floor measurement room of a ~5-m tall, 2-story

building. The ambient sample was taken on the roof by a 2-m long, 12.7-mm OD stainless steel

inlet, and a $PM_{2.5}$ cyclone sampler was also used. The metal tubing was thermally insulated and

135   maintained at a constant temperature of ~25°C. A diffusion drier was also used in-line to dry

136   the relative humidity (RH) of the air sample below 30% before further analysis.

137   **2.2.1 Measurements of relevant species**

138   A TSI-3936 scanning mobility particle sizer (SMPS) and a TSI-3321 aerodynamic particle sizer

139   (APS) were utilized to measure the 10 to 500 nm mobility diameter and 0.5 to 2.5 μm

140   aerodynamic diameter of the PNSD, respectively. The aerodynamic diameters of the APS data

141   were converted into mobility diameters using a material density of 1.7 g cm^{-3}. A detailed data

142   merging method has been described by Cheng et al. (2006). Furthermore, the pipe diffusion

143   loss of SMPS has been corrected using the empirical formula proposed by Kulkarni et al. (1996).

144   An AE-33 Aethalometer (Magee Scientific Inc.) was utilized for BC mass concentration

145   measurement, which was derived from optical attenuation using a mass absorption cross section

146   (MAC) of 7.77 m^2 g^{-1} at 880 nm. The sensitivity of AE-33 was approximately 0.03 μg m^{-3} for

147   a 1-min time resolution and a 5.0 liter per minute (LPM) sample flow rate.

148   The PM$_{2.5}$ mass concentration was measured by an Environment Dust Monitor (Model

149   EDM180, GRIMM Inc.), which monitored the mass concentration of PM$_{2.5}$ and PM$_{10}$

150   simultaneously.

151   Water-soluble ions (potassium (K$^+$), calcium (Ca^{2+}), magnesium (Mg^{2+}), chloride (Cl$^-$), sulfate

152   (SO$_4^{2-}$), nitrate (NO$_3^-$), and ammonium (NH$_4^+$)) were measured with the Monitor for AeRosols

153   and Gases in Air (MARGA) (Model ADI2080, Metrohm Inc.), which is an online analyzer for

154   semi-continuous measurements of gases and water-soluble ions in aerosols (Li et al., 2010).

155   The MARGA was automatically calibrated with standard internal solutions during field

156   measurement. The MARGA utilized its own PM$_{2.5}$ sampling system provided by the

157   manufacturer.

158   The OC mass concentration was measured by a Sunset online OC/EC analyzer (Model RT-4)

159   with a laser transmittance-based charring correction (Wu et al., 2018). The sample flow rate of

160   the OC/EC analyzer was maintained at 8 LPM. For each measurement cycle (one hour),

161   samples were collected onto a quartz filter within the first 45 min and then thermal-optically

162   analyzed during the remaining 15 min. First, OC was completely volatized in oxygen-free

163   helium with a stepwise ramped temperature (600 °C and 840 °C). In the second stage, the

164   temperature was reduced to 550 °C, and then EC and pyrolyzed carbon (PC) were combusted

165   in an oxidizing atmosphere (10% oxygen in helium), while the temperature was increased up

166   to 870 °C step by step. The CO_2 converted from all of the carbon components was then

167   quantified by a nondispersive infrared absorption CO_2 sensor (Lin et al., 2009). An internal

168   calibration peak made by 5% methane in helium was applied to quantify OC and EC. To correct

169   the PC converted from OC to EC, a tunable pulsed diode laser beam was used to monitor the

170   laser transmittance through the quartz filter throughout the thermal-optical analysis (Bauer et

171   al., 2012).

172   **2.2.2 Measurements of optical properties**

173   Light extinction by aerosols at 532 nm was detected using a cavity ring-down aerosol extinction

174   spectrometer (CRDS) (Model XG-1000, Hexin Inc.) by measuring the decay times of laser

175   intensity through the aerosol-containing sample and the filtered background air sample under

176   the same conditions. The extinction coefficient (σ_{ext}) was calculated using the procedure

177   described by Khalizov et al. (2009).

178   Aerosol total scattering (σ_{sp}) was measured by a TSI-3563 integrated nephelometer at three

179   wavelengths (i.e., 450 nm, 550 nm, and 700 nm) and was calibrated with CO_2 following the

180   manual instructions. Particle free air was used to check the nephelometer background signal

181   once every two hours. The scattering coefficients at other wavelengths were extrapolated using

182   the following equations:

183
$$SAE = -\frac{ln\left(\sigma_{scat,\lambda_0}\right) - ln\left(\sigma_{scat,550nm}\right)}{ln\left(\lambda_0\right) - ln(550)} \tag{1}$$

184
$$\sigma_{scat}(\lambda) = \sigma_{scat}(550) \cdot \left(\frac{\lambda}{550}\right)^{-SAE} \tag{2}$$

185   where λ_0=450 nm is for wavelengths less than 550 nm and λ_0=700 nm is for wavelengths greater

186   than 550 nm.

187   The Aethalometer is also used for multi-wavelength light absorption measurements in this study.

188   The seven-wavelength aerosol light attenuation coefficients (σ_{ATN}) were converted into aerosol

189   light absorption coefficients (σ_{abs}) using Eq. (3) (Coen et al., 2010), where k is the parameter

190   that accounts for the loading effect, ATN is the light attenuation through the filter with sample

191   loading and C_{ref} is a fixed multiple scattering parameter.

192
$$\sigma_{abs} = \frac{\sigma_{ATN}}{(1 - k \cdot ATN) \cdot C_{ref}} \tag{3}$$

193   The real-time k value was retrieved using the dual-spot loading correction algorithm developed

194 by Drinovec et al. (2015). The detailed formula of ATN can also be found in Drinovec et al.

195 (2015). C_{ref} is considered a constant that strongly depends on the filter matrix effect. However,

196 some studies have suggested that C_{ref} may vary with wavelength (Arnott et al., 2005;Segura et al.,

197 2014). For internal combustion engines and biomass burning, C_{ref} at 370 nm was expected to be

198 approximately 12% and 18% less than C_{ref} at 532 nm for the aerosol component, respectively

199 (Schmid et al., 2006). Different ambient observations also showed that C_{ref} may have regional

200 specificity, even though it was retrieved by the same methodology (Coen et al., 2010). In this

201 study, C_{ref} =3.29 was used in Eq. (3) at each wavelength, and this value was derived from the

202 slope of σ_{ATN} measured by the Aethalometer vs. σ_{abs}, which was deduced from the CRDS and

203 nephelometer measurements. This C_{ref} was also very similar to the C_{ref} of 3.48 determined from

204 an inter-comparison study between an Aethalometer and a photoacoustic soot spectrometer

205 during a field campaign conducted in the PRD region in 2004 (Wu et al., 2009).

206 The BC light absorption at certain wavelengths was derived from the absorption coefficient σ_{abs}

207 according to Beer-Lambert's law, and its variation between different pairs of wavelengths (i.e.,

208 $\sigma_{abs,BC,\lambda}$) is denoted by the absorption Ångström exponent (AAE) equation developed by

209 Ångström (1929):

$$\sigma_{abs,BC,\lambda}= \sigma_{abs,BC,\lambda_0} \times (\lambda_0/ \lambda)^{-AAE_{BC}} \tag{4}$$

211 It has been suggested that the AAE of BC may vary between short and long wavelength ranges

212 (Lack and Cappa, 2010); hence, applying a wavelength-independent AAE_{BC} may lead to

213 uncertainties in the BC absorption calculation from one wavelength to another. In this work,

214 the light absorptions of BC at various wavelengths were retrieved by a modified wavelength-

215 dependent AAE differentiation method conducted by Wang et al. (2018):

$$\sigma_{abs,BC,\lambda_1}=\sigma_{abs,BC,880nm}\times(\frac{880}{\lambda_1})^{AAE_{BC,520-880nm}} \tag{5.1}$$

$$\sigma_{abs,BC,\lambda_2}=\sigma_{abs,BC,880nm}\times(\frac{880}{520})^{AAE_{BC,520-880nm}} \times(\frac{520}{\lambda_2})^{AAE_{BC,370-520nm}} \tag{5.2}$$

218 Here, $\sigma_{abs,BC,\lambda_1}$ represents the absorption coefficient due to only BC greater than 520 nm, and

219 $\sigma_{abs,BC,\lambda_2}$ represents the absorption coefficient of BC less than 520 nm. $AAE_{BC,\lambda_i-\lambda_{i+1}}$ (i=1, 2

220 and 3) represents the AAE of BC between a longer and shorter wavelength at λ_i=880, 520 and

221 370 nm and was calculated as:

$$AAE_{BC,\lambda_i\text{-}\lambda_{i+1}} = -\frac{ln(\sigma_{abs,BC,\lambda_i}) - ln(\sigma_{abs,BC,\lambda_{i+1}})}{ln(\lambda_i) - ln(\lambda_{i+1})} \tag{6}$$

Accordingly, BrC absorption at a certain wavelength λ ($\sigma_{abs,BrC,\lambda}$) was equal to the value of total

aerosol absorption ($\sigma_{abs,\lambda}$) minus BC absorption ($\sigma_{abs,BC,\lambda}$):

$$\sigma_{abs,BrC,\lambda} = \sigma_{abs,\lambda} - \sigma_{abs,BC,\lambda} \tag{7}$$

The light absorption data at 880 nm ($\sigma_{abs,880nm}$) were selected to represent BC absorption

($\sigma_{abs,BC,880nm}$), which shall not be affected by BrC (Drinovec et al., 2015). It has been reported

that the dust-related contributions of PM$_{2.5}$ were normally less than 5% in wintertime in

Guangzhou; therefore, the influence from dust could be negligible in this study (Huang et al.,

2014).

2.2.3 Estimation of AAE$_{BC}$

Traditionally, AAE$_{BC}$ was believed to be close to 1.0 (Bodhaine, 1995), which has been

commonly used for BC measurements (Olson et al., 2015). However, studies have

demonstrated that AAE$_{BC}$ can be affected by the refractive index of coating materials, mixing

state, morphology, and BC core size (Liu et al., 2015). Therefore, using the default AAE$_{BC}$ = 1

may lead to uncertainty in BrC absorption estimation. To obtain the correct AAE$_{BC}$, a series of

Mie theory calculations were conducted using a simplified core-shell model (Bohren and

Huffman, 1983;Wang et al., 2018). We used a modified BHCOAT code and BHMIE code to

calculate the aerosol optical properties of the core-shell and external mixture at different

wavelengths (Cheng et al., 2006). In the Mie theory, a particle is taken as a perfect

homogeneous sphere, and its extinction and scattering efficiencies, $Q_{ext,Mie,\lambda}$ and $Q_{scat,Mie,\lambda}$,

respectively, are expressed as (Mie, 1908;Seinfeld and Pandis, 1998):

$$Q_{ext,Mie,\lambda} = \frac{2}{\alpha^2}\sum_{n=1}^{\infty}[(2n + 1)Re(a_n + b_n)] \tag{8}$$

$$Q_{scat,Mie,\lambda} = \frac{2}{\alpha^2}\sum_{n=1}^{\infty}[(2n + 1)(|a_n|^2 + |b_n|^2)] \tag{9}$$

where $\alpha = \pi D_p/\lambda$ is the size parameter; a_n and b_n are functions of the complex refractive

index (RI) and α in the Riccati-Bessel form, respectively. *Re* in Eq. (8) denotes that only the

real part of RI is taken. The absorption efficiency ($Q_{abs,Mie,\lambda}$) is thus the difference between

the extinction and scattering efficiencies:

$$Q_{abs,Mie,\lambda} = Q_{ext,Mie,\lambda} - Q_{scat,Mie,\lambda} \tag{10}$$

250 Then, the absorption coefficient $\sigma_{abs,Mie,\lambda}$ was obtained by the following (Bricaud and Morel,

251 1986):

$$\sigma_{abs,Mie,\lambda} = \int Q_{abs,Mie,\lambda} \cdot (\tfrac{\pi}{4} D_p^2) \cdot N(\log D_p) \cdot d \log D_p \tag{11}$$

253 where $N(\log D_p)$ is the PNSD function. A two-component parameterization of dry particles,

254 i.e., the BC core and the nonlight-absorbing species, was applied to calculate aerosol optical

255 properties here (Wex et al., 2002). $\widetilde{m}_{core}$ represents the RI of the BC core, and $\widetilde{m}_{non}$ represents

256 the RI of nonlight-absorbing particles.

257 In a realistic atmosphere, some nonlight-absorbing particles may exist independently without

258 BC (Liu et al., 2013; Cheung et al., 2016). In this work, the portion of nonlight-absorbing

259 particles at a certain size (D_p) was determined by our previous measurements at the same site

260 using a Volatility Tandem Differential Mobility Analyzer (V-TDMA), during which completely

261 vaporized (CV) particles at 300°C were referred to as nonlight-absorbing particles that

262 externally mixed with other BC-containing particles. Thus, the PNSD of CV particles

263 ($N(logD_p)_{CV}$) and BC-containing particles ($N(logD_p)_{BC}$) can be given by the following

264 equations:

$$N(logD_p)_{CV} = N(logD_p)_{measure} \cdot \Phi(D_p)_{N,CV} \tag{12}$$

$$N(logD_p)_{BC} = N(logD_p)_{measure} \cdot (1 - \Phi(D_p)_{N,CV}) \tag{13}$$

267 where $N(logD_p)_{measure}$ is the PNSD of the measured particles from SMPS and APS.

268 $\Phi(D_p)_{N,CV}$ was the number fraction of CV particles in different size bin.

269 A previous study applied three kinds of BC mixture models to calculate the aerosol optical

270 properties, including external, homogenously internal and core-shell mixtures (Bohren and

271 Huffman, 2007;Seinfeld and Pandis, 1998). To quantify the mixing state of BC, r_{ext} was defined

272 as the mass fraction of externally mixed BC (M_{ext}) in total BC (M_{BC}):

$$r_{ext} = \frac{M_{ext}}{M_{BC}} \tag{14}$$

274 Tan et al. (2016) suggested that two extreme conditions of external and core-shell mixtures

275 comprised the actual mixing state of BC in the PRD. Hence, we simply divided the PNSD of

276 BC into the PNSD from an external mixture of BC and a core-shell mixture of BC. The PNSDs

277   of externally mixed BC particles and core-shell mixed BC particles were referred to by the

278   following equations with a given r_{ext}.

279
$$N(logD_p)_{ext} = N(logD_p)_{BC} \cdot f_{BC} \cdot r_{ext} \qquad (15)$$

280
$$N(logD_p)_{core-shell} = N(logD_p)_{BC} \cdot (1 - f_{BC} \cdot r_{ext}) \qquad (16)$$

281   f_{BC} was defined as the BC volume fraction in the BC-containing particle volume, which can be

282   converted from the BC mass concentration:

283
$$f_{BC} = \frac{M_{BC}}{\rho_{BC} \cdot \Sigma_{D_P} N(logD_p)_{BC} \cdot (\frac{\pi}{6} \cdot D_p^3)} \qquad (17)$$

284   where ρ_{BC} is the density of BC and is assumed to be 1.5 g cm^{-3} (Ma et al., 2012); M_{BC} is the BC

285   mass concentration derived from the multi-angle absorption photometer (MAAP), which was

286   obtained by an empirical formula from the Aethalometer that measured the BC concentration

287   ($M_{BC,AE}$), as proposed by Wu et al. (2009):

288
$$M_{BC} = 0.897 \cdot M_{BC, AE} - 0.062 \qquad (18)$$

289   The PNSDs of externally mixed nonlight-absorbing particles and externally mixed BC particles

290   were input into the BHMIE code, and the PNSD of the core-shell mixed particles was imported

291   into the BHCOAT code. Another critical parameter for the core-shell model was the diameter

292   of the BC core. For the simplified core-shell model we applied, the visualization was that a

293   homogeneous BC core sphere was encapsulated in a shell of non-absorbing coating (Bohren

294   and Huffman, 2007). Without size-resolved coating thickness measurements, core-shell mixed

295   particles simply assumed that cores with the same diameter had the same coating thickness.

296   Therefore, the diameter of the BC core was calculated as follows:

297
$$D_{core} = D_p \cdot (\frac{f_{BC} - f_{BC} \cdot r_{ext}}{1 - f_{BC} \cdot r_{ext}})^{\frac{1}{3}} \qquad (19)$$

298   D_{core} and D_p are inputted as parameters into a_n and b_n, respectively, which was described by

299   Bohren and Huffman (2007). Thus, the $\sigma_{abs,BC,Mie, \lambda_i}$ values of all six wavelengths were

300   calculated through the Mie model, and then the AAE$_{BC}$ values of those five wavelengths were

301   obtained using Eq. (6). The performance of this empirically determined calculation method has

302   been compared with other possible BC mixing schemes in details (see Table 1).

303   **2.2.4 Atmospheric radiative transfer model**

304   In this work, theSanta Barbara DISORT Atmospheric Radiative Transfer (SBDART) model

305   was employed to estimate the DRF of BrC absorption, i.e., its effects on the downward and

306 upward fluxes (F in W m^{-2}) of solar radiation at the TOA. SBDART is a software tool that can

307 be used to compute plane-parallel radiative transfer under both clear and cloudy conditions

308 within the atmosphere. More details about this model have been described by Ricchiazzi et al.

309 (1998). Both ground measurements and remote sensing data were used in the simulation. The

310 surface albedo was derived from a 500 m resolution MODIS BRDF/albedo model parameter

311 product (MCD43A3, daily). The MCD43A3 products are the total shortwave broadband black-

312 sky albedo (α_{BSA}) and white-sky albedo (α_{WSA}), while the actual surface albedo (α) was

313 computed from a linear combination of α_{WSA} and α_{BSA}, which were weighted by the diffuse ratio

314 (r_d) and direct ratio ($1-r_d$), respectively:

315
$$\alpha = (1 - r_d) \cdot \alpha_{BSA} + r_d \cdot \alpha_{WSA} \tag{20}$$

316 r_d was obtained from an exponential fit of Eq. (21) based on empirical observations (Stokes and

317 Schwartz, 1994;Roesch, 2004):

318
$$r_d = 0.122 + 0.85e^{-4.8\mu_0} \tag{21}$$

319 where μ_0 is the cosine of the zenith angle, which is calculated by the model for any specified

320 date, time, and latitude and longitude of the site. The surface-based aerosol optical properties,

321 including the aerosol light absorption coefficients of both BC and BrC, i.e., differentiated from

322 each other under the assumption of uniform AAE_{BC}, along with the nephelometer-measured

323 aerosol scattering coefficients, were used to calculate the SSA at different wavelengths

324 according to Eq. (22),

325
$$SSA(\lambda) = \frac{\sigma_{scat, \lambda}}{\sigma_{abs, BrC,\lambda} + \sigma_{abs, BC,\lambda} + \sigma_{scat,\lambda}} \tag{22}$$

326 which was then used in the model calculation. Finally, the AOD and asymmetry factor (ASY)

327 at 440, 675 and 870 nm were derived from the Aerosol Robotic Network (AERONET)

328 measurements at the Hong Kong Polytechnic University site (Holben et al., 1998), which is

329 approximately 115 km to the southeast of the Panyu site. The tropical atmospheric profile was

330 used in the SBDART model based on the prevailing weather conditions in the PRD. The aerosol

331 DRF (ΔF) was calculated as the difference between the downward and upward radiation fluxes:

332
$$\Delta F = F\downarrow - F\uparrow \tag{23}$$ **3 Results and discussion**

333 **3.1 Aerosol light absorption**

334 The AAE_{BC} is widely defined as the uniform representation of the wavelength dependence of a

335 BC particle (Olson et al., 2015). In reality, AAE_{BC} may vary significantly with BC containing

336 aerosols of different sizes, mixing states, and morphologies (Scarnato et al., 2013;Lack and

337 Langridge, 2013). In fact, some studies showed that the AAE of a large-size, pure BC core may

338 be less than 1.0 (Liu et al., 2018) and that the AAE of BC coated with a non-absorbing shell

339 may be larger than that under uniformity (Lack and Cappa, 2010).

340 It has been suggested that a significant fraction of smaller size particles is non BC-containing

341 (Ma et al., 2017;Cheung et al., 2016). BC and non-BC materials can also be externally or

342 internally mixed. Although size resolved BC measurements were not available during this work,

343 we have conducted size resolved Volatility Tandem Differential Mobility Analyzer (V-TDMA)

344 measurements at 300℃ for 40, 80, 110, 150, 200 and 300 nm, respectively, during an earlier

345 field campaign (February 2014) at the same site as in this work. At 300℃, all non-BC particle

346 will be completely vaporized (CV) and thus the portion of non BC particles at such size, denoted

347 as $\Phi_{N,CV}$, can be determined. The average $\Phi_{N,CV}$ values were 0.384, 0.181, 0.180, 0.158, 0.143

348 and 0.137, corresponding to 40, 80, 110, 150, 200 and 300 nm, respectively (Cheung et al.,

349 2016). For particle size larger than 300 nm and less than 40 nm, $\Phi_{N,CV}$ values were set to 0.137

350 and 0.384, respectively. Accordingly, the complete distribution of $\Phi_{N,CV}$ for the whole PNSD

351 was obtained. The mixing states of BC particles were also estimated here, i.e., the mass portion

352 of externally mixed BC with respect to total BC, denoted as r_{ext}. The value of r_{ext} was taken as

353 0.58, which was obtained using an optical closure method during a previous field experiment

354 at this site (Tan et al., 2016a). During the following Mie theory calculation, a fixed refractive

355 index ($\widetilde{m}_{core}$=1.80-0.54i, $\widetilde{m}_{non}$=1.55-10^{-7}i) was adopted for the whole size range. Accordingly,

356 the calculated BC absorption at 880 nm (Abs_{880}) was 21.869 Mm^{-1}, which is reasonably close

357 to the measured mean value of 21.199 Mm^{-1}. To further validate our calculation scheme (Base

358 Case), we have considered several extreme cases. Case 1: BC is completely externally mixed

359 with non-BC particles, i.e., $\Phi_{N,CV}$ = 0 and r_{ext} = 1; Case 2: BC is present in every size bin and

360 BC is completely internally mixed with non-BC material, i.e., $\Phi_{N,CV}$ = 0 and r_{ext} = 0; Case 3:

361 BC is both internally and externally mixed but there is no non BC-containing particles, i.e.,

362 $\Phi_{N,CV}$ = 0 and r_{ext} = 0.58; Case 4: BC is internally mixed with non-BC material and there is non-

363 BC particles present, i.e., $\Phi_{N,CV}$ ranges from 0.384 to 0.137 and r_{ext} = 0; Case 5: the same as

364 case 4 except assuming a fixed non-BC to BC ratio of 0.5, i.e., $\Phi_{N,CV}$ = 0.5, r_{ext} = 0; Case 6: the

365   same as case 5 except that some externally mixed BC is also present, i.e., $\Phi_{N,CV} = 0.5$, $r_{ext} =$

366   0.58. The calculation results are listed in Table 1. Evidently, case 1 (complete externally mixed)

367   will significantly underestimate the measured Abs_{880}, indicating that most BC particles were

368   not likely externally mixed at the Panyu site. Complete internal mixing state (case 2, 4, and 5),

369   on the contrary, would substantially overestimate the BC absorption regardless the form of BC

370   core distribution function. However, when the r_{ext} were considered (case base, 3, and 6), the

371   calculated Abs_{880} values were all very close to the measured value.

372   When the AAE_{BC} was assumed to be uniform, the campaign-averaged σ_{BrC} values were

373   17.6±13.7 Mm^{-1} at 370 nm, 9.7±7.9 Mm^{-1} at 470 nm, 5.8±5.1 Mm^{-1} at 520 nm, 4.0±3.5 Mm^{-1} at

374   590 nm and 2.3±2.1 Mm^{-1} at 660 nm. At the corresponding wavelengths, BrC absorption

375   contributed 26.2±8.5%, 20.0±7.3%, 14.3±6.5%, 11.7±5.3%, and 7.8±4.1% to the total aerosol

376   absorption, respectively. When the AAE_{BC} was applied as the result of the Mie model

377   calculation, the corrected campaign-averaged $\sigma_{abs,BrC}$ values were 23.5±17.7 Mm^{-1} at 370 nm,

378   11.8±9.5 Mm^{-1} at 470 nm, 6.7±5.7 Mm^{-1} at 520 nm, 4.6±3.9 Mm^{-1} at 590 nm and 2.6±2.3 Mm^{-}

379   ^{1} at 660 nm. At the corresponding wavelengths, BrC absorption contributed 34.1±8.0%,

380   23.7±7.3%, 16.0±6.7%, 13.0±5.4%, and 8.7±4.3% to the total aerosol absorption (see Fig. 2),

381   respectively. Evidently, aerosol light absorption was predominantly due to BC; however, BrC

382   also played a significant role, especially at shorter wavelengths. Table 2 shows the

383   intercomparison of BrC light absorption in the near UV range between this work and other

384   studies in the East Asian region. Clearly, the reported values vary substantially, and our result

385   is toward the lower end of values.

386   **3.2 Uncertainty in BC and BrC optical differentiation**

387   Theoretically, the magnitude of BC absorptions can be affected by both parts of the complex

388   refractive indexes (RIs); thus, AAE_{BC} may also vary with the RIs of both the BC core and

389   coating shell. In fact, RI was also one of the least known properties of BC and other coating

390   materials with negligible absorbing capabilities. The refractive index of the BC core ($\tilde{m}_{core}$)

391   displays a wide range of variations (Liu et al., 2018). Typically, the real and imaginary parts of

392   the RI can vary from 1.5 to 2.0 and 0.5 to 1.1, respectively. In addition, the shell was assumed

393   to consist of non-absorbing material in the core-shell model, i.e., its imaginary RI was set to be

394   close to zero (10^{-7}). The real part of the non-absorbing material RI ($\tilde{m}_{non}$) may vary from 1.35

395   to 1.6 due to the presence of OA (Zhang et al., 2018;Redmond and Thompson, 2011) and

396   inorganic salts (Erlick et al., 2011). Hence, it is necessary to investigate the uncertainties

397   associated with the variations in AAE_{BC} by varying the RIs of both the BC core and the non-

398   absorbing materials.

399   Figure 3 shows the impacts of RI on the evaluations of AAE_{BC} based on core-shell and external

400   configuration, where the RI of the BC core was set to be constant, i.e., $\widetilde{m}_{core}$=1.80-0.54i, and

401   the real part of $\widetilde{m}_{non}$ varied from 1.35 to 1.6 at an interval of 0.05, with the imaginary part of

402   $\widetilde{m}_{non}$ set at 10^{-7}. As shown in Fig. 3a, the calculated AAE_{BC} for the core-shell model was higher

403   than 1.0 at longer wavelengths (520 to 880 nm) and lower than 1.0 at shorter wavelengths (370

404   to 520 nm) (the red line in Fig. 3 denotes AAE_{BC}=1). The averaged $AAE_{BC,370-520nm}$ ranged from

405   0.84 to 0.87, and the $AAE_{BC,520-880nm}$ ranged from 1.07 to 1.15, indicating that the $AAE_{BC,520-}$

406   $_{880nm}$ appeared to be more sensitive to the shell's real part than $AAE_{BC,370-520nm}$. Even if the shell

407   material was assumed to be non-absorbing, the variation in the real RI of the shell, which was

408   referred to as the real part of $\widetilde{m}_{non}$, still led to changes in the shell's refractivity and

409   correspondingly altered its lensing effect, causing a change in AAE_{BC}. Meanwhile, $AAE_{BC,370-}$

410   $_{520nm}$ and $AAE_{BC,520-880nm}$ generally increased with an increasing real part of the shell. In Fig. 3b,

411   under the externally mixed conditions, $AAE_{BC,370-520nm}$ and $AAE_{BC,520-880nm}$ were both less than

412   1.0. The average $AAE_{BC,370-520nm}$ was 0.33, and the average $AAE_{BC,520-880nm}$ was 0.63. These

413   values were far less than the values under core-shell mixture conditions. In the external mixture

414   model, the BC core and nonlight-absorbing materials were assumed to exist dependently, and

415   then the optical properties of these two components were considered separately. Therefore,

416   altering the real part of the externally mixed non-absorbing material would not affect the light

417   absorption property of the BC core or AAE_{BC}.

418   The impacts of the BC core on AAE_{BC} are shown in Fig. 4, where the refractive index of

419   nonlight-absorbing materials was assumed to be $\widetilde{m}_{non}$=1.55-$10^{-7}i$ and $\widetilde{m}_{non}$ was wavelength-

420   independent. Fig. 4 was obtained with a core-shell mixture model (Fig. 4a and 4b) and an

421   external mixture model (Fig. 4c and 4d) by varying the real part of $\widetilde{m}_{core}$ from 1.5 to 2.0 with

422   a step of 0.05 and varying the imaginary part of the $\widetilde{m}_{core}$ from 0.4 to 1.0 with a step of 0.05,

423   respectively. As shown in Figs. 4a and 4b, for the core-shell mixture, the averaged $AAE_{BC,370-}$

424   $_{520nm}$ ranged from 0.55 to 0.99, and the averaged $AAE_{BC,520-880nm}$ ranged from 0.84 to 1.27. The

425 AAE$_{BC}$ at a certain wavelength generally increased when increasing the real part of $\widetilde{m}_{core}$ but

426 decreased when increasing the imaginary part of $\widetilde{m}_{core}$. The AAE$_{BC}$ appeared to be more

427 sensitive to the imaginary part of $\widetilde{m}_{core}$ than the real part of $\widetilde{m}_{core}$ because the imaginary part

428 of $\widetilde{m}_{core}$ was directly related to the light-absorbing properties of particles. In Fig. 4c and 4d,

429 for the external mixture, the averaged AAE$_{BC,370-520nm}$ ranged from 0.04 to 0.45 and the averaged

430 AAE$_{BC,520-880nm}$ ranged from 0.28 to 0.79, while the averaged AAE$_{BC,370-520nm}$ and AAE$_{BC,520-880nm}$

431 were both less than 1.0. Similar to the core-shell mixture, the AAE$_{BC,520-880nm}$ increased

432 when increasing the real part of $\widetilde{m}_{core}$ but decreased when increasing the imaginary part of

433 $\widetilde{m}_{core}$. However, the variation patterns of AAE$_{BC,370-520nm}$ were different from those of AAE$_{BC,520-880nm}$.

434 $_{880nm}$. The AAE$_{BC,370-520nm}$ values were not changed by altering the real part of $\widetilde{m}_{core}$ within the

435 low imaginary part of $\widetilde{m}_{core}$, whereas the AAE$_{BC,370-520nm}$ values still increased when increasing

436 the real part of $\widetilde{m}_{core}$ within the high imaginary part of $\widetilde{m}_{core}$. A possible explanation was that

437 the externally mixed BC core had weak light absorption within the low imaginary part of $\widetilde{m}_{core}$,

438 causing the AAE$_{BC,370-520nm}$ values to be insensitive to the real part of $\widetilde{m}_{core}$. The AAE$_{BC,520-880nm}$

439 $_{880nm}$ values were higher than the AAE$_{BC,370-520nm}$ values regardless of whether in they were for

440 the core-shell mixture or external mixture. In addition, the AAE$_{BC}$ values conducted by the

441 core-shell mixture were higher than those conducted by the external mixture.

442 Figure 4 demonstrates that the variation in the imaginary RI of the BC core has the most

443 significant impact on the estimated AAE$_{BC}$, indicating that the chemical component of BC

444 emitted from different sources leads to a large uncertainty in AAE$_{BC}$ estimation. At the same

445 time, the influence arising from varying the real RI of the BC core was relatively moderate.

446 Nevertheless, Fig. 3 demonstrated that change in the real RI of the non-absorbing materials

447 caused the least/no impact compared to that caused by the variations in the complex RI of the

448 BC core.

449 We want to note that most BC-containing particles are often observed as fractal rather than

450 spherical in shape (Katrinak et al., 1993). Because the Mie model assumes that all particles are

451 spherical, it may lead to potential uncertainty for the estimation of AAE$_{BC}$ and BrC absorption

452 contributions. Moreover, the externally mixed soot aggregates were "chain-like" or "puff-like"

453 in the PRD dry season (Feng et al., 2010), in which the fractal dimension (D$_f$) was between 1.5

454 and 2.0. Coating soot aggregates were likely sphere (D$_f$ approaches 3) from the high-resolution

455 transmission electron microscopy (TEM) measurements taken in Hongkong ((Zhou et al.,

456 2014)). A soot aggregate sensitivity study with the superposition T-matrix method indicated

457 that using the assumption of volume-equivalent spheres for the soot aggregates may result in

458 an overestimation of approximately up to 15% and an underestimation of approximately up to

459 50% in the predicted 870 nm light absorption when the D_f is between 1.5 and 3.0 (Liu et al.,

460 2008). However, we should recognize the fact that different shapes or BC core positions may

461 bring more difficult computational problems in practical numerical simulations. Applying the

462 simplified Mie model would be a tradeoff scheme without particulate material morphological

463 measurements in Panyu.

464 **3.3 Characteristics of BrC light absorption, water-soluble ions and OC concentrations**

465 Globally, BrC has been observed to be highly correlated with biomass and biofuel burning

466 emissions (Laskin et al., 2015). Since large quantities of sylvite are present in biomass burning

467 particles, the K^+ abundance has often been used as a biomass burning tracer (Levine, 1991).

468 Figure 5 presents the time series of the OC mass concentration, K^+ concentration, and BrC

469 absorption from 29 November 2014 to 2 January 2015 at the Panyu site. The range of the OC

470 concentration obtained from the OC/EC online analyzer was from 1.5 to 65.2 μg cm$^{-3,}$ and the

471 campaign average was 12.5±7.3 μg cm^{-3}. The BrC absorption hourly mean data were between

472 0.2 and 123.2 Mm$^{-1,}$ and the campaign average was 23.5±17.7 Mm^{-1}. On the other hand, the

473 average K^+ concentration was 1.0 ± 0.7 μg cm^{-3} (ranging from 0 to 5.4 μg cm^{-3}). Clearly, similar

474 trends among OC, K^+, and BrC absorption can be seen during this field campaign (Fig. 5).

475 To investigate the origins of these observed OC, K^+, and BrC, wind rose plots (as shown in Fig.

476 6) were generated for OC, K^+, and BrC absorption, respectively. All three panels of Fig. 6

477 consistently show that the three substances were associated with the same wind pattern. For the

478 entire campaign period, the highest values of OC, K^+, and $\sigma_{abs,BrC,370nm}$ were mostly associated

479 with southwesterly winds with a relatively low wind speed (~2 m s^{-1}). The relatively higher OC

480 and K^+ concentrations were highly related to the seasonal straw burning in the countryside of

481 the PRD located to the west of the Panyu station. In contrast, OC and K^+ concentrations during

482 periods with easterly winds were substantially lower than those during periods with westerly

483 winds. The wind rose plot of $\sigma_{abs,BrC,370nm}$ is shown in Fig. 6c. Similar to OC and K^+, $\sigma_{abs,BrC,370nm}$

484 showed higher values under weak (<2 m s^{-1}) westerly winds and lower values from the north

485   and south, indicating that BrC absorption was likely attributed to local sources and was

486   accumulated under calm wind conditions. However, there was a detectable difference among

487   the three rose plots in the maximum concentration direction. A possible explanation was that

488   although biomass burning emissions were believed to be the dominant and primary source of

489   OC, K^+, and BrC, their emission ratios were highly variable and may change with the type of

490   biofuel and burning condition and may even vary during different stages of burning (Burling et

491   al., 2012). Although biomass burning emissions contain substantial light-absorbing BrC,

492   further atmospheric aging processes may significantly reduce its light-absorbing capability

493   (Satish et al., 2017). Moreover, secondary formation may also lead to BrC formation inside

494   these primary aerosols, such as humic-like substances formed through aqueous-phase reactions,

495   which have been suggested to be an important component of BrC (Andreae and Gelencser,

496   2006).

497   To further explore the possible sources of BrC optical absorption, the diurnal variations in OC,

498   K^+, $\sigma_{abs,BrC,370nm}$, and $\sigma_{abs,BrC,370nm}$ /OC values are plotted in Fig. 7. The diurnal variation in OC

499   at the Panyu site appeared to be dominated by the development of the planetary boundary layer

500   (PBL) height, i.e., primary emissions accumulated at night and were swiftly diluted by vertical

501   mixing in the morning. The slight increase in OC in the afternoon indicated that photochemistry

502   may have still weakly contributed to SOA formation. Figure 7b shows the diurnal variation in

503   K^+. Unlike OC, K^+ shows a small peak at approximately 6 AM, which was consistent with

504   breakfast time and was very likely due to cooking activities using biofuel. No lunch and dinner

505   time K^+ peaks were observed. The most likely explanation is that the boundary layer height is

506   much higher during lunch and dinner time than in the early morning, providing a much better

507   atmospheric diffusion condition for air pollutants. It is still a common practice to collect straw

508   as biofuel in local rural areas, which can be visually spotted but is not heavily utilized in the

509   region. However, the diurnal profile of $\sigma_{abs,BrC,370nm}$ (see Fig. 7c) shows the combined features

510   of OC and K^+ since both primary and secondary processes affect its intensity. The nighttime

511   increasing trend was most likely attributed to straw burning activities in early winter in nearby

512   rural areas that continued to accumulate within the shallow PBL (Jiang et al., 2013).

513   $\sigma_{abs,BrC,370nm}$/OC, i.e., the mass absorption coefficient of BrC (MAC_{BrC}) (Fig. 7d), showed a

514   relatively flat pattern, with a pronounced dip in the afternoon and higher values at nighttime,

515 which was likely due to enhanced primary emissions and stable stratification at nighttime.

516 Declining trends during the late morning and afternoon hours indicated that the aging process

517 and photochemical production may reduce the light-absorbing capacity of BrC (Qin et al.,

518 2018).

519 Furthermore, Fig. 8 shows the linear regression analysis results used to evaluate the correlations

520 of $\sigma_{abs,BrC,370nm}$ with the OC, K^+, Ca^{2+}, Mg^{2+}, Cl^-, SO_4^{2-}, NO_3^-, and NH_4^+ concentrations. The best

521 correlations can be found between $\sigma_{abs,BrC,370nm}$ and K^+ (R^2=0.6148), followed by those between

522 $\sigma_{abs,BrC,370nm}$ and OC (R^2=0.4514), NO_3^- (R^2=0.4224) and NH_4^+ (R^2=0.4656). Source

523 apportionment analysis of OA and BrC absorption in Beijing and Guangzhou illustrated that

524 biomass burning organic aerosols (BBOAs) correlated well with BrC light absorption (Xie et

525 al., 2018;Qin et al., 2018). Thus, the significant correlation between BrC absorption and K^+

526 reaffirmed that biomass burning was the crucial emission source of BrC observed in this work.

527 Although the geographic location of the observation site was situated in a coastal area and K^+

528 could also be found in sea salt (Pio et al., 2008), it should be noted that the prevailing wind

529 direction during winter was from the north (see Fig. 3), which drives maritime air parcels away

530 from the site. Hence, the effect of sea salt and crustal materials to K^+ was slight, which was

531 demonstrated in the supplementary information as shown in Fig. S1. Other earlier studies also

532 suggested that the sea salt contribution to the K^+ concentrations of $PM_{2.5}$ was trivial in the PRD

533 region during the winter (Lai et al., 2007). Another possible K^+ source was coal combustion.

534 The coal consumption in the PRD region was dominated by coal-fired power plants. The

535 emission from power plants was usually very steady and was less likely to affect the diurnal

536 correlation between K^+ and BrC absorption. As shown in Fig. 9, the ratios of $K^+/PM_{2.5}$ varies

537 approximately from 0.015 and 0.020 and the diurnal profile of $K^+/PM_{2.5}$ shows very little

538 variation. Yu et al. (2018) have suggested that K^+ usually accounted for 2.34-5.49% of $PM_{2.5}$ in

539 the laboratory biomass burning study. However, K^+ was normally lower than 1% of coal

540 combustion $PM_{2.5}$. Therefore, the ratio range of K^+ to $PM_{2.5}$ observed in this work likely

541 indicated aged biomass burning particles. Both nitrogen oxides (NO_x) and ammonia (NH_3) can

542 be found in biomass burning plumes (Andreae and Merlet, 2001). For NO_3^- and NH_4^+, nitrate

543 can be converted from NO_x through atmospheric reactions, and ammonium may originate from

544 NH_3. However, similar to the diurnal variation in $\sigma_{abs,BrC,370nm}$, diurnal variations in NH_4^+ and

545 NO_3^- also increased in the afternoon and appeared at nighttime in Fig 9. However, $NO_3^-/PM_{2.5}$

546 and $NH_4^+/PM_{2.5}$ reached their peaks at noon, indicating that ammonium nitrate formed from the

547 secondary reaction at this time. Along with the reduced boundary layer height and ambient

548 temperature, NO_3^- was accumulated until the photochemical reaction stopped at night. The

549 diurnal variation in NH_4^+ was similar to that in NO_3^- due to the acid/base neutralization reaction.

550 The overlapping of the $\sigma_{abs,BrC,370nm}$, NH_4^+ and NO_3^- diurnal variations would lead to a significant

551 correlation between BrC absorption and NO_3^- or NH_4^+. High concentrations of Ca^{2+} and Mg^{2+}

552 are often found in dust-related aerosols (Lee et al., 1999). $\sigma_{abs,BrC,370nm}$ showed poor correlations

553 with both Ca^{2+} and Mg^{2+}, indicating that dust-related aerosol components contribute

554 insignificantly to the total aerosol mass loading and, thus, dust may not affect the AAE

555 differentiation method used in this work. Although sulfur dioxide (SO_2) may also be emitted by

556 biomass burning, SO_4^{2-} is often believed to be secondary in nature, and the presence of other

557 intense SO_2 sources (e.g., automobile and industrial emissions) further reduces the correlation

558 between BrC and SO_4^{2-}. Sources of Cl^- include both combustion and sea salt spray (Waldman

559 et al., 1991). Although the prevailing wintertime wind direction was from the north, sea salt

560 can still be carried to the site by a weak sea breeze, and thus, Cl^- may not show considerable

561 correlation with BrC.

562 **3.4 BrC radiative forcing efficiency**

563 The radiative effects of aerosol scattering, BrC absorption, and BC absorption were investigated

564 by the SBDART model. For each investigated variable under cloud-free conditions, we run the

565 model twice to calculate the DRF at the TOA with and without the investigated variable.

566 Accordingly, the difference of ΔF between the two simulations was considered as the radiative

567 effect of the investigated variable. The results showed that the average radiative forcings at the

568 TOA by scattering, BrC absorption, and BC absorption were -21.4±5.5 W m^{-2}, 2.3±1.8 W m^{-2},

569 and 10.9±5.1 W m^{-2}, respectively. Furthermore, BrC absorption was attributed to 15.8±4.4%

570 of the warming effect caused by aerosol light absorption, demonstrating the nonnegligible role

571 of BrC in radiative forcing evaluation.

572 We also calculated the BrC radiative forcing efficiency (RFE) under various *SSA* (ranging from

573 0.7 to 0.99) at three wavelengths, i.e., 440 nm, 675 nm, and 870 nm. The RFE was denoted as

574 the radiative forcing normalized by the AOD. The average AOD and ASY at the three

575 wavelengths were 0.365 and 0.691 at 440 nm, 0.212 and 0.632 at 675 nm, and 0.154 and 0.619

576 at 870 nm, respectively. A solar zenith angle of 55° and an average shortwave broadband surface

577 albedo (0.119) were used in the calculation. The results were plotted as a set of RFE lookup

578 charts as a function of the surface BrC absorption contribution (see Fig. 10).

579 In general, for any wavelength, the RFE increased with increasing BrC absorption contribution

580 for a certain SSA, indicating that BrC was a more efficient radiative forcing agent due to the

581 preferential absorbance of BrC in a shorter wavelength range. However, for a certain BrC

582 absorption contribution, the RFE increased with decreasing SSA, i.e., a higher portion of light-

583 absorbing aerosol components can lead to more efficient radiative forcing. The trend among

584 panels (a), (b), and (c) in Fig. 10 demonstrated that the effect of BrC absorption contribution

585 on RFE was wavelength-dependent, i.e., BrC was a weaker radiative forcing agent at longer

586 wavelengths, which is also consistent with the wavelength-dependent light-absorbing property

587 of BrC. The red stars in Fig. 10 denote the average SSA and BrC absorption contribution

588 conditions during this campaign, i.e., 0.029 W m^{-2} per unit AOD at 440 nm (Fig. 10a), 0.007

589 W m^{-2} per unit AOD at 675 nm (Fig. 10b), and 0.0002 W m^{-2} per unit AOD at 870 nm (Fig.

590 10c). These results suggested that the average value of RFE decreased distinctly from 440 nm

591 to 870 nm not only because of the lower BrC absorption contribution but also because of the

592 wavelength-dependence of the BrC RFE. It should also be noted that the simulations were based

593 on SSA measured under dry conditions. Under the typical ambient conditions of the PRD, the

594 SSA might be markedly enhanced by aerosol water uptake (Jung et al., 2009), and then, the BrC

595 radiative forcing efficiency might be less. Moreover, Fig. 10 also serves as a lookup table to

596 conveniently assess the BrC radiative forcing efficiency at different wavelengths with different

597 BrC absorption contributions for a certain SSA.

598 **4 Conclusion**

599 In this work, light absorption due to BrC in the PRD region of China was quantitatively deduced

600 during the winter season of 2014. Using the absorption coefficients of BC calculated according

601 to the Mie theory and the observed total aerosol absorption coefficients, we estimated the

602 AAE$_{BC}$ and hence the BrC absorption contribution for the optically equivalent mixture

603 configuration. The average BrC light absorption contribution ranged from 8.7±4.3% at 660 nm

604 up to 34.1±8.0% at 370 nm when AAE$_{BC}$ was set as uniform. The sensitivity of AAE$_{BC}$

estimation associated with different RI and mixing state assumptions was further investigated. The results showed that variations in the real RI of the non-absorbing material (1.35 to 1.6) may decrease $AAE_{BC,370-520nm}$ from 0.84 to 0.87 and $AAE_{BC,520-880nm}$ from 1.07 to 1.15 for core-shell mixtures, with an $AAE_{BC,370-520nm}$ of 0.33 and $AAE_{BC,520-880nm}$ of 0.63 for external mixtures. Variations in the core's real RI (1.5 to 2.0) and imaginary RI (0.4 to 1.0) may reduce $AAE_{BC,370-520nm}$ from 0.55 to 0.99 and $AAE_{BC,520-880nm}$ from 0.84 to 1.27 for the core-shell mixture and reduce $AAE_{BC,370-520nm}$ from 0.04 to 0.45 and $AAE_{BC,520-880nm}$ from 0.28 to 0.79 for the external mixture. These results indicate that the optical properties of the BC core and non-absorbing material can significantly affect the accuracy of AAE_{BC} and corresponding BrC absorption contribution estimations.

Additionally, the measurements of major water-soluble inorganic ions (including K^+, NO_3^-, and NH_4^+) and particulate OC showed consistent features with those of $\sigma_{abs,BrC,370nm}$, implying that BrC was associated with biomass-burning emissions from nearby rural areas. Moreover, the diurnal trend in $\sigma_{abs,BrC,370nm}$/OC indicated that primary biomass burning emissions can produce intense light-absorbing BrC, while the photochemical aging process may weaken the light-absorbing capability of BrC.

Using a radiative transfer model (i.e., SBDART), we estimated the BrC effects on aerosol radiative forcing. The average shortwave aerosol direct radiative forcings due to scattering, BrC absorption, and BC absorption at the TOA were evaluated to be -21.4±5.5 W m^{-2}, 2.3±1.8 W m^{-2}, and 10.9±5.1 W m^{-2}, respectively. BrC absorption accounted for 15.8±4.4% of the total shortwave solar absorption warming effect at the TOA, indicating that BrC might be an important climate forcing agent, which is largely neglected in current climate models. To facilitate the estimation of the climate effects of BrC, a set of look-up charts was constructed for the investigated area based on the default tropical atmosphere profile, average surface albedo, average asymmetry factor, and surface-measured aerosol properties (i.e., BrC absorption contribution, *SSA*, and AOD). Therefore, the role of the BrC radiative forcing efficiency at three wavelengths can be conveniently assessed for certain *SSA* and BrC absorption contributions.

Author contributions

635 HT, JZ, YM, and CC designed the experiments, and ZL, LL, YQ, NW, FL, YL, and MC carried

636 out the field measurements and data analysis. ZL and YQ performed Mie theory simulation.

637 ZL, JZ, and HT prepared the manuscript with comments from all coauthors.

638

639 *Acknowledgements*

640 This work is supported by the National Key Project of MOST (2016YFC0201901 and

641 2016YFC0203305), and National Natural Science Foundation of China (41575122 and

642 41730106). We are also deeply thankful for Dr. Wu and the staff at the Hong Kong Polytechnic

643 University site of AERONET.

644

645 **References:**

646 Andreae, M. O., and Merlet, P.: Emission of trace gases and aerosols from biomass burning,
647 Glob. Biogeochem. Cycle, 15, 955-966, 2001.

648 Andreae, M. O., and Gelencser, A.: Black carbon or brown carbon? The nature of light-
649 absorbing carbonaceous aerosols, Atmospheric Chemistry & Physics, 6, 3131-3148, 2006.

650 Ångström, A.: On the Atmospheric Transmission of Sun Radiation and on Dust in the Air,
651 Geografiska Annaler, 11, 156-166, 1929.

652 Arnott, W. P., Hamasha, K., Moosmüller, H., Sheridan, P. J., and Ogren, J. A.: Towards Aerosol
653 Light-Absorption Measurements with a 7-Wavelength Aethalometer: Evaluation with a
654 Photoacoustic Instrument and 3-Wavelength Nephelometer, Aerosol Science and Technology,
655 39, 17-29, 10.1080/027868290901972, 2005.

656 Arola, A., Schuster, G. L., Pitkänen, M. R. A., Dubovik, O., Kokkola, H., Lindfors, A. V.,
657 Mielonen, T., Raatikainen, T., Romakkaniemi, S., Tripathi, S. N., and Lihavainen, H.: Direct
658 radiative effect by brown carbon over the Indo-Gangetic Plain, Atmospheric Chemistry and
659 Physics, 15, 12731-12740, 10.5194/acp-15-12731-2015, 2015.

660 Bauer, J. J., Yu, X.-Y., Cary, R., Laulainen, N., and Berkowitz, C.: Characterization of the
661 Sunset Semi-Continuous Carbon Aerosol Analyzer, Journal of the Air & Waste Management
662 Association, 59, 826-833, 10.3155/1047-3289.59.7.826, 2012.

663 Bodhaine, B. A.: Aerosol absorption measurements at Barrow, Mauna Loa and the south pole,
664 Journal of Geophysical Research Atmospheres, 100, 8967–8975, 1995.

665 Bohren, C. F., and Huffman, D. R.: Wiley: Absorption and Scattering of Light by Small
666 Particles - Craig F. Bohren, Donald R. Huffman, Optics & Laser Technology, 31, 328-328, 1983.

667 Bohren, C. F., and Huffman, D. R.: Absorption and Scattering of Light by Small Particles,

668   WILEY‑VCH Verlag GmbH & Co. KGaA 328-328 pp., 2007.

669   Bond, T. C., Streets, D. G., Yarber, K. F., Nelson, S. M., Woo, J. H., and Klimont, Z.: A
670   technology-based global inventory of black and organic carbon emissions from combustion, J.
671   Geophys. Res.-Atmos., 109, 43, 10.1029/2003jd003697, 2004.

672   Bond, T. C., Zarzycki, C., Flanner, M. G., and Koch, D. M.: Quantifying immediate radiative
673   forcing by black carbon and organic matter with the Specific Forcing Pulse, Atmospheric
674   Chemistry and Physics, 11, 1505-1525, 10.5194/acp-11-1505-2011, 2011.

675   Bricaud, A., and Morel, A.: Light attenuation and scattering by phytoplanktonic cells: a
676   theoretical modeling, Applied Optics, 25, 571, 10.1364/ao.25.000571, 1986.

677   Burling, I. R., Yokelson, R. J., Akagi, S. K., Urbanski, S. P., Wold, C. E., Griffith, D. W. T.,
678   Johnson, T. J., Reardon, J., and Weise, D. R.: Airborne and ground-based measurements of the
679   trace gases and particles emitted by prescribed fires in the United States (vol 11, pg 12197,
680   2011), Atmospheric Chemistry and Physics, 12, 103-103, 10.5194/acp-12-103-2012, 2012.

681   Chan, C. K., and Yao, X.: Air pollution in mega cities in China, Atmospheric Environment, 42,
682   1-42, http://dx.doi.org/10.1016/j.atmosenv.2007.09.003, 2008.

683   Cheng, Y., He, K. B., Zheng, M., Duan, F. K., Du, Z. Y., Ma, Y. L., Tan, J. H., Yang, F. M., Liu,
684   J. M., Zhang, X. L., Weber, R. J., Bergin, M. H., and Russell, A. G.: Mass absorption efficiency
685   of elemental carbon and water-soluble organic carbon in Beijing, China, Atmospheric
686   Chemistry and Physics, 11, 11497-11510, 10.5194/acp-11-11497-2011, 2011.

687   Cheng, Y. F., Eichler, H., Wiedensohler, A., Heintzenberg, J., Zhang, Y. H., Hu, M., Herrmann,
688   H., Zeng, L. M., Liu, S., Gnauk, T., Brüggemann, E., and He, L. Y.: Mixing state of elemental
689   carbon and non-light-absorbing aerosol components derived from in situ particle optical
690   properties at Xinken in Pearl River Delta of China, Journal of Geophysical Research:
691   Atmospheres, 111, doi:10.1029/2005JD006929, 2006.

692   Cheung, H. H. Y., Tan, H., Xu, H., Li, F., Wu, C., Yu, J. Z., and Chan, C. K.: Measurements of
693   non-volatile aerosols with a VTDMA and their correlations with carbonaceous aerosols in
694   Guangzhou, China, Atmospheric Chemistry and Physics, 16, 8431-8446, 10.5194/acp-16-
695   8431-2016, 2016.

696   Coen, M. C., Weingartner, E., Apituley, A., Ceburnis, D., Fierzschmidhauser, R., Flentje, H.,
697   Henzing, J. S., Jennings, S. G., Moerman, M., and Petzold, A.: Minimizing light absorption
698   measurement artifacts of the Aethalometer: evaluation of five correction algorithms,
699   Atmospheric Measurement Techniques, 3, 457-474, 2010.

700   Desyaterik, Y., Sun, Y., Shen, X., Lee, T., Wang, X., Wang, T., and Collett, J. L.: Speciation of
701   "brown" carbon in cloud water impacted by agricultural biomass burning in eastern China,
702   Journal of Geophysical Research: Atmospheres, 118, 7389-7399, 10.1002/jgrd.50561, 2013.

703   Drinovec, L., Močnik, G., Zotter, P., Prévôt, A. S. H., Ruckstuhl, C., Coz, E., Rupakheti, M.,

704 Sciare, J., Müller, T., Wiedensohler, A., and Hansen, A. D. A.: The "dual-spot" Aethalometer:
705 an improved measurement of aerosol black carbon with real-time loading compensation,
706 Atmospheric Measurement Techniques, 8, 1965-1979, 10.5194/amt-8-1965-2015, 2015.

707 Erlick, C., Abbatt, J. P. D., and Rudich, Y.: How Different Calculations of the Refractive Index
708 Affect Estimates of the Radiative Forcing Efficiency of Ammonium Sulfate Aerosols, Journal
709 of the Atmospheric Sciences, 68, 1845-1852, 10.1175/2011jas3721.1, 2011.

710 Feng, X., Dang, Z., Huang, W., Shao, L., and Li, W.: Microscopic morphology and size
711 distribution of particles in PM2.5 of Guangzhou City, J Atmos Chem, 64, 37-51,
712 10.1007/s10874-010-9169-7, 2010.

713 Feng, Y., Ramanathan, V., and Kotamarthi, V. R.: Brown carbon: a significant atmospheric
714 absorber of solar radiation?, Atmospheric Chemistry and Physics, 13, 8607-8621, 10.5194/acp-
715 13-8607-2013, 2013.

716 Hoffer, A., Gelencsér, A., Guyon, P., and Kiss, G.: Optical properties of humic-like substances
717 (HULIS) in biomass-burning aerosols, Atmospheric Chemistry & Physics, 5, 3563-3570, 2005.

718 Holben, B. N., Eck, T. F., Slutsker, I., Tanré, D., Buis, J. P., Setzer, A., Vermote, E., Reagan, J.
719 A., Kaufman, Y. J., and Nakajima, T.: AERONET—A Federated Instrument Network and Data
720 Archive for Aerosol Characterization, Remote Sensing of Environment, 66, 1-16, 1998.

721 Huang, R.-J., Zhang, Y., Bozzetti, C., Ho, K.-F., Cao, J.-J., Han, Y., Daellenbach, K. R., Slowik,
722 J. G., Platt, S. M., Canonaco, F., Zotter, P., Wolf, R., Pieber, S. M., Bruns, E. A., Crippa, M.,
723 Ciarelli, G., Piazzalunga, A., Schwikowski, M., Abbaszade, G., Schnelle-Kreis, J.,
724 Zimmermann, R., An, Z., Szidat, S., Baltensperger, U., Haddad, I. E., and Prévôt, A. S. H.:
725 High secondary aerosol contribution to particulate pollution during haze events in China,
726 Nature, 514, 218-222, 10.1038/nature13774, 2014.

727 Jiang, D., Wang, C., Wu, D., Deng, X., Huang, X., Tan, H., Li, F., and Deng, T.: Diurnal
728 variation of atmospheric boundary layer over Wushan station, Guangzhou using wind profiler
729 radar (in Chinese), Journal of Tropical Meteorology, 29, 129-135, 2013.

730 Jung, J., Lee, H., Kim, Y. J., Liu, X., Zhang, Y., Gu, J., and Fan, S.: Aerosol chemistry and the
731 effect of aerosol water content on visibility impairment and radiative forcing in Guangzhou
732 during the 2006 Pearl River Delta campaign, Journal of Environmental Management, 90, 3231-
733 3244, http://dx.doi.org/10.1016/j.jenvman.2009.04.021, 2009.

734 Katrinak, K. A., Rez, P., Perkes, P. R., and Buseck, P. R.: Fractal geometry of carbonaceous
735 aggregates from an urban aerosol, Environmental Science & Technology, 27, págs. 225-238,
736 1993.

737 Khalizov, A. F., Xue, H., Wang, L., Zheng, J., and Zhang, R.: Enhanced light absorption and
738 scattering by carbon soot aerosol internally mixed with sulfuric acid, The journal of physical
739 chemistry. A, 113, 1066-1074, 10.1021/jp807531n, 2009.

740 Kirchstetter, T. W., Novakov, T., and Hobbs, P. V.: Evidence that the spectral dependence of
741 light absorption by aerosols is affected by organic carbon, Journal of Geophysical Research:
742 Atmospheres, 109, n/a-n/a, 10.1029/2004jd004999, 2004.

743 Kulkarni, P., Baron, P. A., and Willeke, K.: Aerosol measurement : principles, techniques, and
744 applications, Van Nostrand Reinhold, 807-808 pp., 1996.

745 Lack, D. A., and Cappa, C. D.: Impact of brown and clear carbon on light absorption
746 enhancement, single scatter albedo and absorption wavelength dependence of black carbon,
747 Atmospheric Chemistry and Physics, 10, 4207-4220, 10.5194/acp-10-4207-2010, 2010.

748 Lack, D. A., and Langridge, J. M.: On the attribution of black and brown carbon light absorption
749 using the Ångström exponent, Atmospheric Chemistry and Physics, 13, 10535-10543,
750 10.5194/acp-13-10535-2013, 2013.

751 Lai, S.-c., Zou, S.-c., Cao, J.-j., Lee, S.-c., and Ho, K.-f.: Characterizing ionic species in PM2.5
752 and PM10 in four Pearl River Delta cities, South China, Journal of Environmental Sciences, 19,
753 939-947, https://doi.org/10.1016/S1001-0742(07)60155-7, 2007.

754 Laskin, A., Laskin, J., and Nizkorodov, S. A.: Chemistry of atmospheric brown carbon, Chem
755 Rev, 115, 4335-4382, 10.1021/cr5006167, 2015.

756 Lee, E., Chan, C. K., and Paatero, P.: Application of positive matrix factorization in source
757 apportionment of particulate pollutants in Hong Kong, Atmospheric Environment, 33, 3201-
758 3212, https://doi.org/10.1016/S1352-2310(99)00113-2, 1999.

759 Levine, J.: Biomass Burning Aerosols in a Savanna Region of the Ivory Coast, French Forum,
760 235-236, 1991.

761 Li, H., Han, Z., Cheng, T., Du, H., Kong, L., Chen, J., Zhang, R., and Wang, W.: Agricultural
762 Fire Impacts on the Air Quality of Shanghai during Summer Harvesttime, Aerosol and Air
763 Quality Research, 10.4209/aaqr.2009.08.0049, 2010.

764 Lin, P., Hu, M., Deng, Z., Slanina, J., Han, S., Kondo, Y., Takegawa, N., Miyazaki, Y., Zhao,
765 Y., and Sugimoto, N.: Seasonal and diurnal variations of organic carbon in PM2.5in Beijing
766 and the estimation of secondary organic carbon, Journal of Geophysical Research, 114,
767 10.1029/2008jd010902, 2009.

768 Liu, C., Chung, C. E., Yin, Y., and Schnaiter, M.: The absorption Ångström exponent of black
769 carbon: from numerical aspects, Atmospheric Chemistry and Physics, 18, 6259-6273,
770 10.5194/acp-18-6259-2018, 2018.

771 Liu, D., Taylor, J. W., Young, D. E., Flynn, M. J., Coe, H., and Allan, J. D.: The effect of
772 complex black carbon microphysics on the determination of the optical properties of brown
773 carbon, Geophysical Research Letters, 42, 613-619, 2015.

774 Liu, L., Mishchenko, M. I., and Patrick Arnott, W.: A study of radiative properties of fractal

775 soot aggregates using the superposition T-matrix method, Journal of Quantitative Spectroscopy
776 and Radiative Transfer, 109, 2656-2663, 10.1016/j.jqsrt.2008.05.001, 2008.

777 Ma, N., Zhao, C. S., Müller, T., Cheng, Y. F., Liu, P. F., Deng, Z. Z., Xu, W. Y., Ran, L., Nekat,
778 B., van Pinxteren, D., Gnauk, T., Müller, K., Herrmann, H., Yan, P., Zhou, X. J., and
779 Wiedensohler, A.: A new method to determine the mixing state of light absorbing carbonaceous
780 using the measured aerosol optical properties and number size distributions, Atmos. Chem.
781 Phys., 12, 2381-2397, 10.5194/acp-12-2381-2012, 2012.

782 Ma, Y., Li, S. Z., Zheng, J., Khalizov, A., Wang, X., Wang, Z., and Zhou, Y. Y.: Size-resolved
783 measurements of mixing state and cloud-nucleating ability of aerosols in Nanjing, China, J.
784 Geophys. Res.-Atmos., 122, 9430-9450, 10.1002/2017jd026583, 2017.

785 Mie, G.: Beitrage Zur Optik Truber Medien, Speziell Kolloidaler Metallosungen, Annalen Der
786 Physik, 25, 377, 1908.

787 Moosmüller, H., Chakrabarty, R. K., Ehlers, K. M., and Arnott, W. P.: Absorption Ångström
788 coefficient, brown carbon, and aerosols: basic concepts, bulk matter, and spherical particles,
789 Atmospheric Chemistry and Physics, 11, 1217-1225, 10.5194/acp-11-1217-2011, 2011.

790 Nakayama, T., Ikeda, Y., Sawada, Y., Setoguchi, Y., Ogawa, S., Kawana, K., Mochida, M.,
791 Ikemori, F., Matsumoto, K., and Matsumi, Y.: Properties of light‐absorbing aerosols in the
792 Nagoya urban area, Japan, in August 2011 and January 2012: Contributions of brown carbon
793 and lensing effect, Journal of Geophysical Research Atmospheres, 119, 12,721-712,739, 2015.

794 Olson, M. R., Victoria Garcia, M., Robinson, M. A., Van Rooy, P., Dietenberger, M. A., Bergin,
795 M., and Schauer, J. J.: Investigation of black and brown carbon multiple-wavelength-dependent
796 light absorption from biomass and fossil fuel combustion source emissions, Journal of
797 Geophysical Research: Atmospheres, 120, 6682-6697, 10.1002/2014jd022970, 2015.

798 Pio, C. A., Legrand, M., Alves, C. A., Oliveira, T., Afonso, J., Caseiro, A., Puxbaum, H.,
799 Sanchez-Ochoa, A., and Gelencsér, A.: Chemical composition of atmospheric aerosols during
800 the 2003 summer intense forest fire period, Atmospheric Environment, 42, 7530-7543, 2008.

801 Qin, Y. M., Tan, H. B., Li, Y. J., Li, Z. J., Schurman, M. I., Liu, L., Wu, C., and Chan, C. K.:
802 Chemical characteristics of brown carbon in atmospheric particles at a suburban site near
803 Guangzhou, China, Atmospheric Chemistry and Physics Discussions, 1-23, 10.5194/acp-2018-
804 730, 2018.

805 Redmond, H., and Thompson, J. E.: Evaluation of a quantitative structure-property relationship
806 (QSPR) for predicting mid-visible refractive index of secondary organic aerosol (SOA),
807 Physical chemistry chemical physics : PCCP, 13, 6872-6882, 10.1039/c0cp02270e, 2011.

808 Ricchiazzi, P., Yang, S., Gautier, C., and Sowle, D.: SBDART: A Research and Teaching
809 Software Tool for Plane-Parallel Radiative Transfer in the Earth's Atmosphere, Bulletin of the
810 American Meteorological Society, 79, 2101-2114, 10.1175/1520-
811 0477(1998)079<2101:Sarats>2.0.Co;2, 1998.

812 Roesch, A.: Use of Moderate-Resolution Imaging Spectroradiometer bidirectional reflectance
813 distribution function products to enhance simulated surface albedos, Journal of Geophysical
814 Research, 109, 10.1029/2004jd004552, 2004.

815 Sareen, N., Schwier, A. N., Shapiro, E. L., Mitroo, D., and McNeill, V. F.: Secondary organic
816 material formed by methylglyoxal in aqueous aerosol mimics, Atmospheric Chemistry and
817 Physics, 10, 997-1016, 10.5194/acp-10-997-2010, 2010.

818 Satish, R., Shamjad, P., Thamban, N., Tripathi, S., and Rastogi, N.: Temporal Characteristics of
819 Brown Carbon over the Central Indo-Gangetic Plain, Environ Sci Technol, 51, 6765-6772,
820 10.1021/acs.est.7b00734, 2017.

821 Scarnato, B. V., Nielsen, K., Vahidinia, S., and Richard, D.: Effect of Aggregation and Mixing
822 on optical properties of Black Carbon, 2013.

823 Schmid, O., Artaxo, P., Arnott, W. P., Chand, D., Gatti, L. V., Frank, G. P., Hoffer, A., Schnaiter,
824 M., and Andreae, M. O.: Spectral light absorption by ambient aerosols influenced by biomass
825 burning in the Amazon Basin. I: Comparison and field calibration of absorption measurement
826 techniques, Atmos. Chem. Phys., 6, 3443-3462, 10.5194/acp-6-3443-2006, 2006.

827 Segura, S., Estellés, V., Titos, G., Lyamani, H., Utrillas, M. P., Zotter, P., Prévôt, A. S. H.,
828 Močnik, G., Alados-Arboledas, L., and Martínez-Lozano, J. A.: Determination and analysis of
829 in situ spectral aerosol optical properties by a multi-instrumental approach, Atmospheric
830 Measurement Techniques, 7, 2373-2387, 10.5194/amt-7-2373-2014, 2014.

831 Seinfeld, J. H., and Pandis, S. N.: Atmospheric Chemistry and Physics, John Wiley & Sons, Inc,
832 New York, 1998.

833 Stokes, G. M., and Schwartz, S. E.: The Atmospheric Radiation Measurement (ARM) Program:
834 Programmatic Background and Design of the Cloud and Radiation Test Bed, Bulletin of the
835 American Meteorological Society, 75, 1201–1221, 1994.

836 T. C. Bond, †, M. Bussemer, B. Wehner, S. Keller, R. J. Charlson, a., and Heintzenberg‡, J.:
837 Light Absorption by Primary Particle Emissions from a Lignite Burning Plant, Environmental
838 Science & Technology, 33, 3887-3891, 1999.

839 Tan, H., Liu, L., Fan, S., Li, F., Yin, Y., Cai, M., and Chan, P. W.: Aerosol optical properties and
840 mixing state of black carbon in the Pearl River Delta, China, Atmospheric Environment, 131,
841 196-208, http://dx.doi.org/10.1016/j.atmosenv.2016.02.003, 2016a.

842 Tan, H., Yin, Y., Li, F., Liu, X., Chan, P. W., Deng, T., Deng, X., Wan, Q., and Wu, D.:
843 Measurements of particle number size distributions and new particle formations events during
844 winter in the Pearl River Delta region, China, Journal of Tropical Meteorology, 22, 191-199,
845 10.16555/j.1006-8775.2016.02.009, 2016b.

846 Waldman, J. M., Lioy, P. J., Zelenka, M., Jing, L., Lin, Y. N., He, Q. C., Qian, Z. M., Chapman,
847 R., and Wilson, W. E.: Wintertime measurements of aerosol acidity and trace elements in

848   Wuhan, a city in central China, Atmospheric Environment. Part B. Urban Atmosphere, 25, 113-
849   120, https://doi.org/10.1016/0957-1272(91)90045-G, 1991.

850   Wang, J., Nie, W., Cheng, Y., Shen, Y., Chi, X., Wang, J., Huang, X., Xie, Y., Sun, P., Xu, Z.,
851   Qi, X., Su, H., and Ding, A.: Light absorption of brown carbon in eastern China based on 3-
852   year multi-wavelength aerosol optical property observations and an improved absorption
853   Ångström exponent segregation method, Atmospheric Chemistry and Physics, 18, 9061-9074,
854   10.5194/acp-18-9061-2018, 2018.

855   Washenfelder, R. A., Attwood, A. R., Brock, C. A., Guo, H., Xu, L., Weber, R. J., Ng, N. L.,
856   Allen, H. M., Ayres, B. R., and Baumann, K.: Biomass burning dominates brown carbon
857   absorption in the rural southeastern United States, Geophysical Research Letters, 42, 653-664,
858   2015.

859   Wex, H., Neusüß, C., Wendisch, M., Stratmann, F., Koziar, C., Keil, A., Wiedensohler, A., and
860   Ebert, M.: Particle scattering, backscattering, and absorption coefficients: An in situ closure
861   and sensitivity study, Journal of Geophysical Research Atmospheres, 107, LAC-1-LAC 4-18,
862   2002.

863   Wu, C., Wu, D., and Yu, J. Z.: Quantifying black carbon light absorption enhancement with
864   a novel statistical approach, Atmospheric Chemistry and Physics, 18, 289-309, 10.5194/acp-
865   18-289-2018, 2018.

866   Wu, D., Mao, J., Deng, X., Tie, X., Zhang, Y., Zeng, L., Li, F., Tan, H., Bi, X., Huang, X., Chen,
867   J., and Deng, T.: Black carbon aerosols and their radiative properties in the Pearl River Delta
868   region, Science in China Series D: Earth Sciences, 52, 1152-1163, 10.1007/s11430-009-0115-
869   y, 2009.

870   Xie, C., Xu, W., Wang, J., Wang, Q., Liu, D., Tang, G., Chen, P., Du, W., Zhao, J., Zhang, Y.,
871   Zhou, W., Han, T., Bian, Q., Li, J., Fu, P., Wang, Z., Ge, X., Allan, J., Coe, H., and Sun, Y.:
872   Vertical characterization of aerosol optical properties and brown carbon in winter in urban
873   Beijing, China, Atmospheric Chemistry and Physics Discussions, 1-28, 10.5194/acp-2018-788,
874   2018.

875   Yu, J., Yan, C., Liu, Y., Li, X., Zhou, T., and Zheng, M.: Potassium: A Tracer for Biomass
876   Burning   in   Beijing?,   Aerosol   and   Air   Quality   Research,   18,   2447-2459,
877   10.4209/aaqr.2017.11.0536, 2018.

878   Yuan, J. F., Huang, X. F., Cao, L. M., Cui, J., Zhu, Q., Huang, C. N., Lan, Z. J., and He, L. Y.:
879   Light absorption of brown carbon aerosol in the PRD region of China, Atmospheric Chemistry
880   and Physics, 16, 1433-1443, 10.5194/acp-16-1433-2016, 2016.

881   Zhang, Y., Li, Z., Sun, Y., Lv, Y., and Xie, Y.: Estimation of atmospheric columnar organic
882   matter (OM) mass concentration from remote sensing measurements of aerosol spectral
883   refractive indices, Atmospheric Environment, 179, 107-117, 10.1016/j.atmosenv.2018.02.010,
884   2018.

885   Zhou, S., Wang, T., Wang, Z., Li, W., Xu, Z., Wang, X., Yuan, C., Poon, C. N., Louie, P. K. K.,
886   Luk, C. W. Y., and Wang, W.: Photochemical evolution of organic aerosols observed in urban
887   plumes from Hong Kong and the Pearl River Delta of China, Atmospheric Environment, 88,
888   219-229, 10.1016/j.atmosenv.2014.01.032, 2014.
889
890

891   **Table 1.** Inter-comparison of the performance of various Mie-calculation schemes. The base

892   case is based on the empirical distribution function and mixing states of BC particles obtained

893   from previous field measurements at the same site. $\Phi_{N,CV}$ denotes the portion of non-BC

894   particles and r_{ext} is the mass portion of externally mixed BC with respect to total BC. AAE_{BC} is

895   the absorption Ångström exponent of BC, and the subscript represents the wavelength range.

896     $Abs_{BrC,370}\%$ and $Abs_{BrC,520}\%$ are the BrC absorption contributions at 370 nm and 520 nm,

897   respectively. $Calcabs_{880}$ is the calculated absorption at 880 nm using Mie model. $Measabs_{880}$ is

898   the measured absorption by an Aethalometer at 880 nm. b is the intercept of the regression

899   analysis between $Measabs_{880}$ and $Calcabs_{880}$, i.e., $Calcabs_{880}=b*\ Measabs_{880}$. R^2 is the

900   correlation coefficient of the equation. The refractive index of BC core ($\widetilde{m}_{core}$) and nonlight-

901   absorbing particles ($\widetilde{m}_{non}$) is set to be $1.80-0.54i$ and $1.55-10^{-7}i$, respectively (Tan et al., 2016a),

Case #	Scheme	$\Phi_{N,CV}$	r_{ext}	$AAE_{BC,370\text{-}520}$	$AAE_{BC,520\text{-}880}$	$Abs_{BrC,370}\%$	$Abs_{BrC,520}\%$	Calc abs$_{880}$	Meas abs$_{880}$	b	R^2
Base		0.384 to 0.137	0.58	0.723	0.962	34.13%	15.96%	21.869		1.019	0.979
1		0	1	0.331	0.626	51.64%	29.57%	15.832		0.747	0.968
2		0	0	0.856	1.128	24.76%	8.28%	27.827		1.295	0.976
3		0	0.58	0.745	0.974	33.22%	15.46%	21.936	**21.199**	1.029	0.979
4		0.384 to 0.137	0	0.835	1.111	26.01%	9.14%	27.302		1.269	0.975
5		0.5	0	0.778	1.043	29.96%	12.30%	24.921		1.150	0.968
6		0.5	0.58	0.674	0.928	36.39%	17.49%	20.897		0.977	0.975

902

903

904

905 **Table 2.** Observational studies of the BrC light absorption coefficient and contribution in the

906 near-ultraviolet wavelength range in East Asia.

Periods	Location	λ (nm)	Mean BrC absorption coefficient	Mean BrC absorption contribution	Instrumentation	Reference
Nov. 2014 – Jan. 2015	Guangzhou (China)	370	17.6 Mm^{-1} 23.5 Mm^{-1}	26.2% (AAE$_{BC}$=1) 34.1% (corrected)	Aethalometer AE-33	This study
Jan. 2014 – Feb. 2014; Sep. 2014 – Oct. 2014	Shenzhen (China)	405	3.0 Mm^{-1} 1.4 Mm^{-1}	11.7% (winter) 6.3% (fall)	PASS-3	Yuan et al. (2016)
Nov. 2014	Heshan (China)	405	3.9 Mm^{-1}	12.1%	PASS-3	Yuan et al. (2016)
Nov. 2016– Dec. 2016	Beijing (China)	370	106.4 Mm^{-1} 93.8 Mm^{-1}	46% (at the ground) 48% (at 260 m)	Aethalometer AE-33	Xie et al. (2018)
Jun. 2013 – May. 2016	Nanjing (China)	370	35.8 Mm^{-1}	16.7%	Aethalometer AE-31	Wang et al. (2018)
Jan. 2012	Nagoya (Japan)	405	Not detected	11% (300°C) 17% (400°C)	Thermodenuder PASS-3	(Nakayama et al. (2015))

907
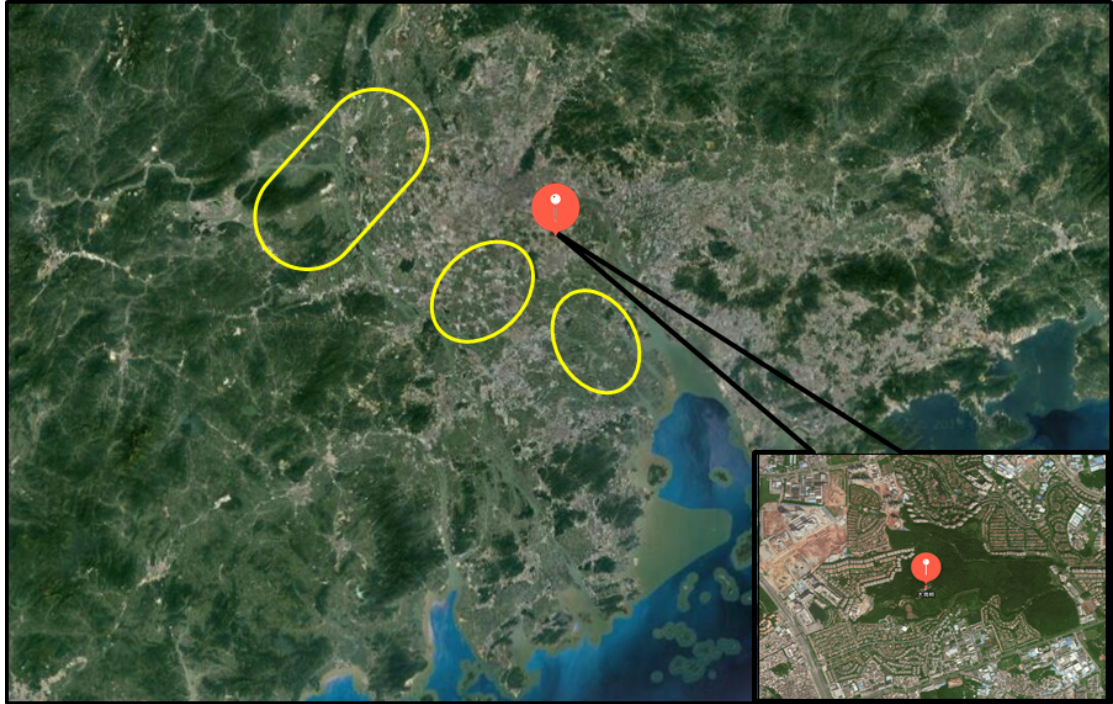
908
909   Figure 1. The location of Panyu station (CAWNET) in the PRD region (indicated by the red

910   dot). The plain areas within the yellow circles are the main rural areas of western PRD.

911

912

913
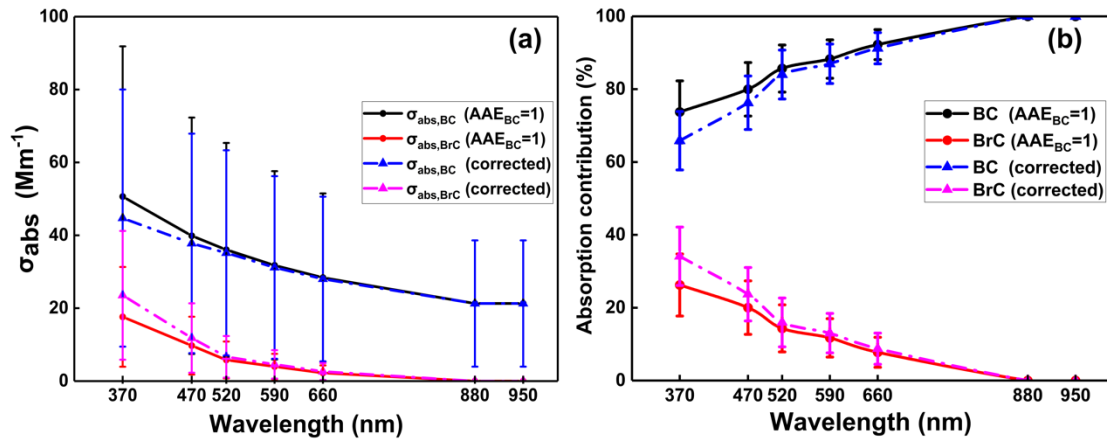
Figure 2. (a) BC and BrC particle average light absorption coefficients at different wavelengths under different AAE_{BC} assumptions; the whiskers represent an error of one standard deviation. (b) Contributions of BC and BrC to the total light absorption coefficient at different wavelengths under different AAE_{BC} assumptions; the whiskers represent an error of one standard deviation.

919
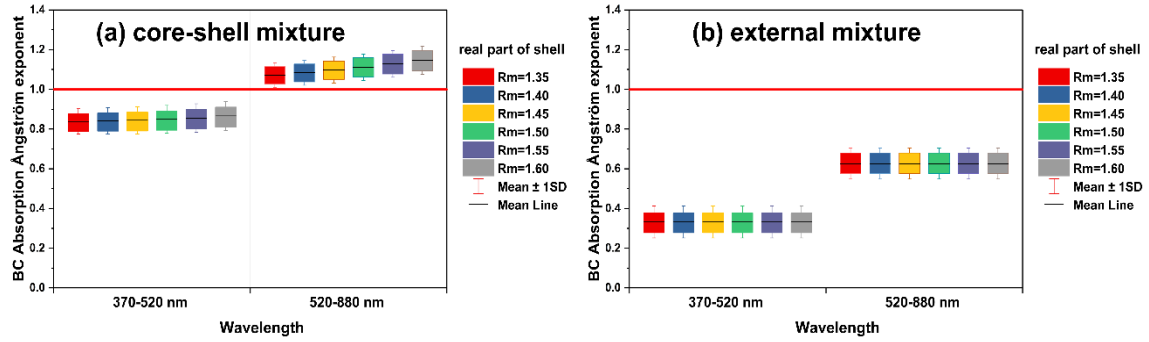
Figure 3. Influence of the wavelength-independent refractive index of the non-absorbing materials on the (a) AAEs of the core-shell mixture and (b) AAEs of the external mixture with a constant BC core refractive index ($\widetilde{m}_{core}$=1.80-0.54i). The imaginary part of the non(less)-absorbing shell was set to 10^{-7}, while the real part varied from 1.35 to1.60. In each panel, the boundaries of the box represent the 75th and 25th percentiles; the whiskers above and below each box indicate an error of one standard deviation; the black lines in the boxes denote the average values. In panels a and b, the red line indicates where AAE_{BC}=1.

929
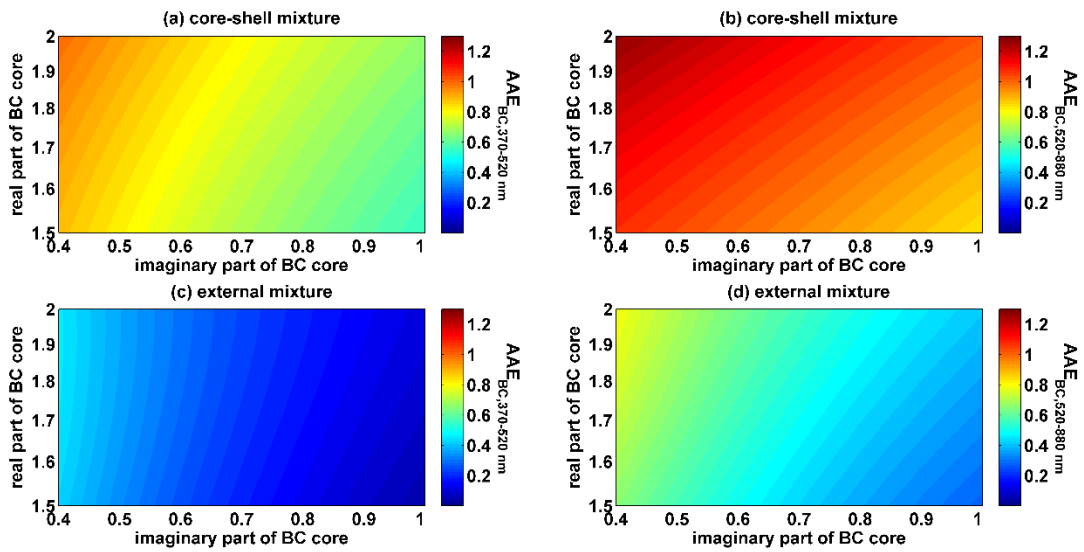
930

931 Figure 4. Influence of the wavelength-independent refractive index of the BC core on

932 AAEs with a constant shell refractive index ($\widetilde{m}_{shell}=1.55-10^{-7}i$). A core-shell mixture

933 was used for panels a and b, and an external mixture was used for panels c and d. The

934 real part of $\widetilde{m}_{core}$ varied from 1.5 to 2.0, with a step of 0.05, and the imaginary part of

935 $\widetilde{m}_{core}$ varied from 0.4 to 1.0, with a step of 0.05.

936
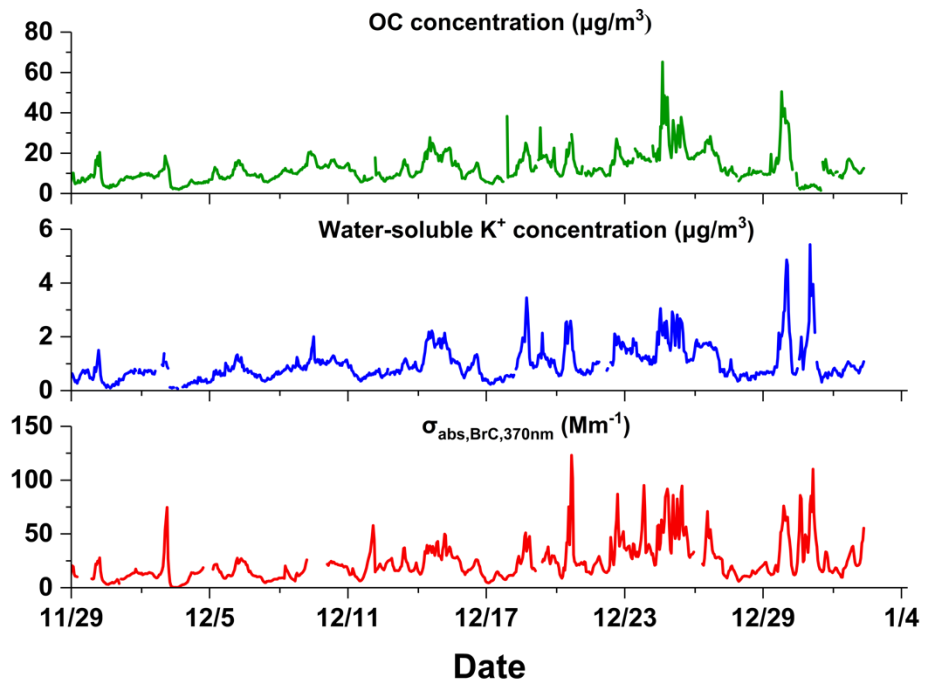
937

938 Figure 5. Time series of the OC aerosol mass concentration (green line), water-soluble K^+ mass

939 concentration (blue line), and BrC light absorption (red line).

940

941

(a) OC concentration (µg/m³) (b) K⁺ concentration (µg/m³) (c) σ$_{abs, BrC, 370nm}$ (Mm⁻¹)
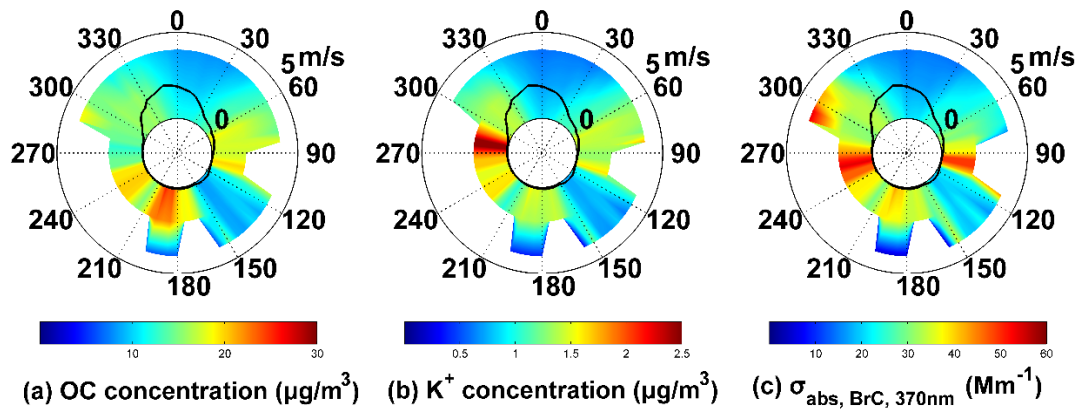
942

943 Figure 6. Wind rose plots of OC (a), K⁺ (b), and $\sigma_{abs,BrC,370nm}$ (c). In each panel, the black solid

944 lines denote the frequency of the wind direction. The shaded contour represents the average

945 values of the corresponding species for that wind speed (radial length) and wind direction

946 (transverse direction) in polar coordinates.

947
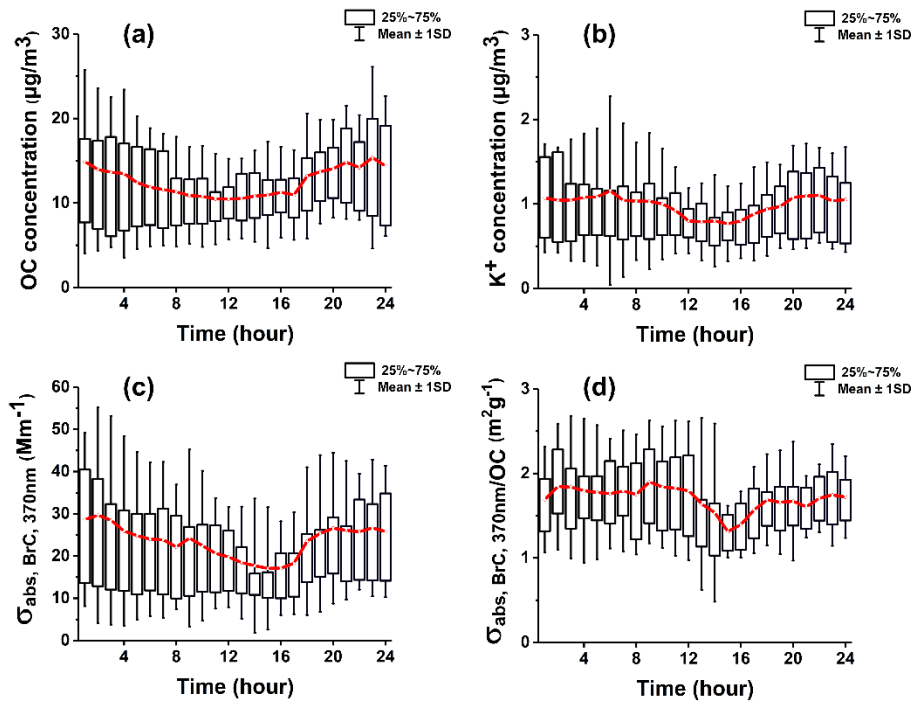
950 Figure 7. Box-whisker plots of diurnal trends in the OC concentration (a), water-soluble K+

951 concentration (b), $\sigma_{abs,BrC,370nm}$ (c), and $\sigma_{abs,BrC,370nm}$ /OC (d). The red traces represent the

952 variation in the average value. The upper and lower boundaries of the box represent the 75th

953 and 25th percentiles, respectively; the whiskers above and below each box represent an error

954 of one standard deviation.

955
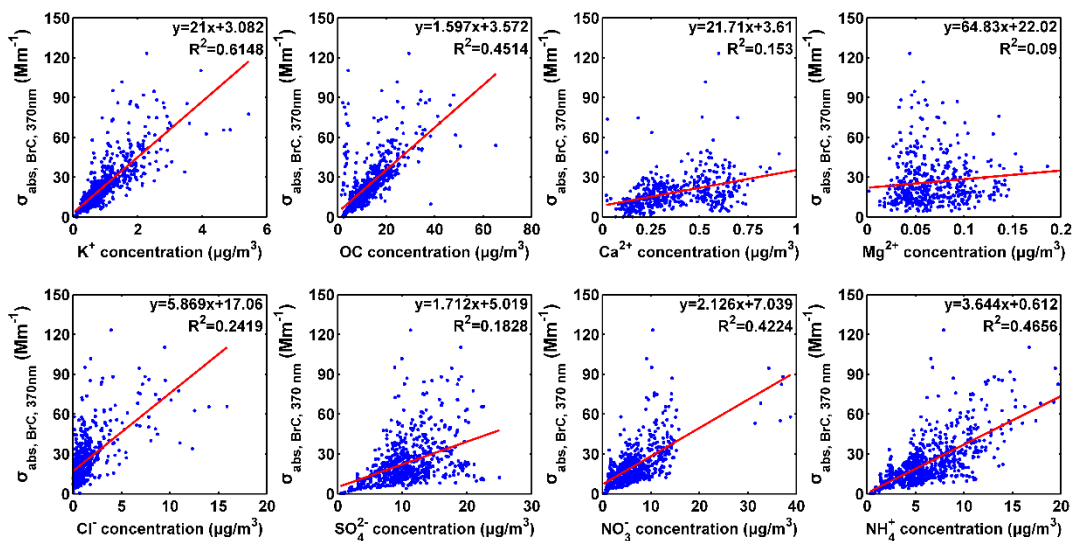
956

957 Figure 8. Correlations of the BrC absorption coefficient at 370 nm with OC, water-soluble K^+,

958 Ca^{2+}, Mg^{2+}, Cl^-, SO_4^{2-}, NO_3^-, and NH_4^+ aerosol concentrations.
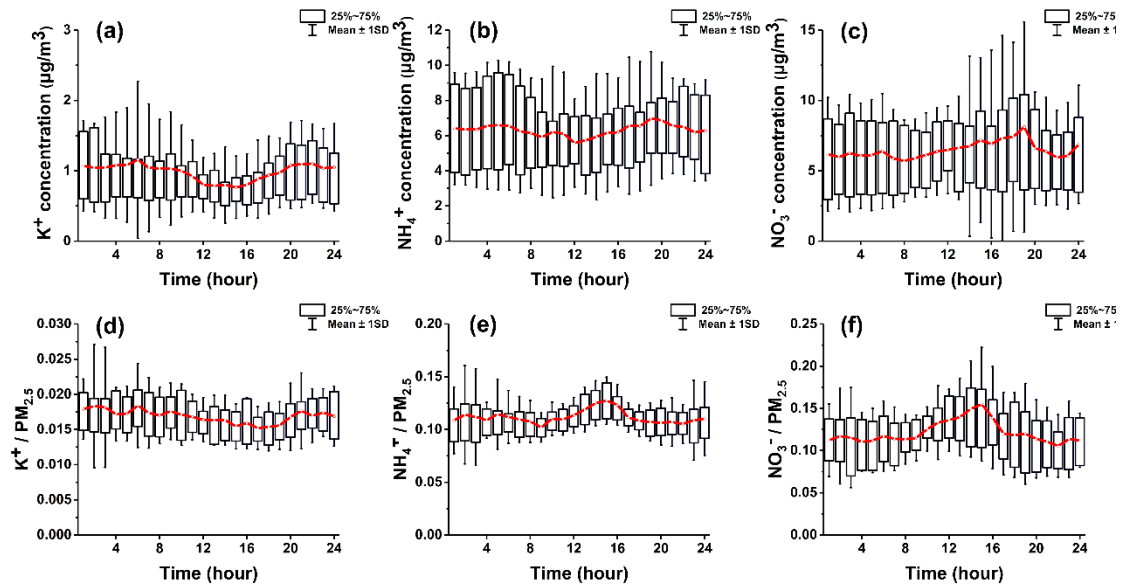
959

960   Figure 9. Box-whisker plots of diurnal trends in K^+ concentration (a), NH_4^+ concentration (b),

961   NO_3^- concentration (c), $K^+/PM_{2.5}$ (d), $NH_4^+/PM_{2.5}$ (e) and $NO_3^-/PM_{2.5}$ (f). The red traces

962   represent the variation in average value. The upper and lower boundaries of the box represent

963   the 75th and 25th percentiles, respectively; the whiskers above and below each box represent

964   an error of one standard deviation.

965

966

967
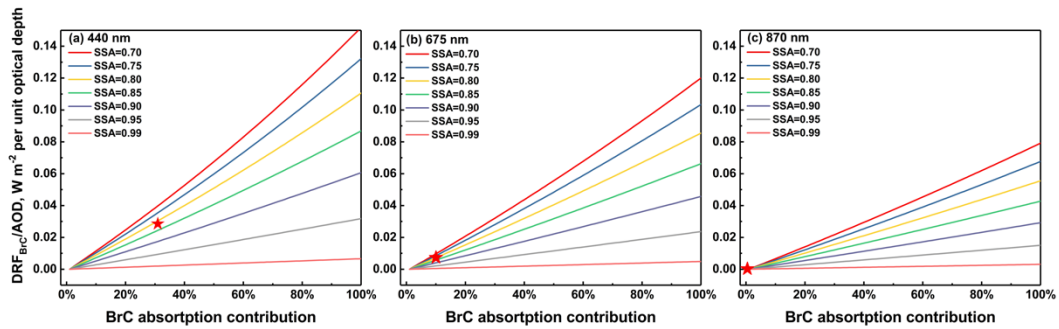
968

969 Figure 10. BrC radiative forcing efficiencies, which are defined as the BrC TOA direct radiative

970 forcing divided by the AOD, as a function of the BrC to BC absorption ratio and *SSA* measured

971 at the surface. The average AOD of the three wavelengths, the average ASY of the three

972 wavelengths, a solar zenith angle of 55°, and average shortwave broadband surface albedo were

973 used in the calculation. The red star corresponds to the average *SSA* and BrC absorption

974 contributions determined from this campaign.